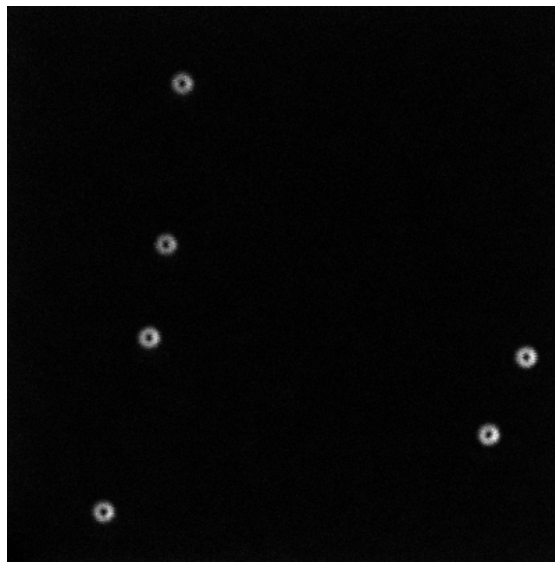# Analysis of STED Doughnuts generated by a Spatial Light Modulator

Author:
A.A.J. (Anton) de Boer

Daily Supervisor:
Dr. G.A. Blab
2nd examiner:
Prof. Dr. P. van der Straten

August 25, 2015

Abstract

This paper summarizes the research done for a master thesis at the Molecular Biophysics group, part the of the Physics Department of Utrecht University. Using a custom microscope set-up, we have researched the effects of polarization on the shape of Stimulated Emission-Depletion doughnuts in a high NA objective, simulating an actual STED environment. Additionally, rather than a vortex phase plate, we have used a Spatial Light Modulator to generate the doughnuts. The results are compared to theoretical predictions resulting from simulations.

1

Contents

Chapter 1

Introduction

After the establishment of the electromagnetic theory of Maxwell in the late 19th century, there was a sense that the medium and speed of light were nature's last remaining secret, where we were confident that we had figured out practically everything else. However, when a solid explanation was finally given by the theory of special relativity, the universe was found to be much more complex than the elegant theories of the physicists of that time would indicate. In that sense, one would not be wrong to say that light has been one of physics greatest adversaries.

Of course, light has also given us the possibility to gain a grasp of the very small when we were introduced to the microscope (besides giving us the ability to observe our surroundings), but even then light has been physics' 'anti-hero' as its wavelike properties have put limits on the minimum resolution of the microscope. Still, this has not stopped scientists to figure a way around lights' properties and overcome these limits in order to image structures much smaller than would be seem possible.

In this thesis we have focused on an increasingly popular microscope technique named Stimulated Emission Depletion, or STED, microscopy where much better resolutions are obtained than with a regular light microscope. As we will see, STED requires a modified focus in the shape of a doughnut, where its shape and size have a large effect on the resolution. Here, we will try to create these doughnuts using a Spatial Light Modulator (SLM). First, we will analyze the effects of a SLM on light, before we use it to create doughnuts. Then, we will analyze the shape and size of the generated doughnuts in a relevant environment, where we also take into account possible effects on the light's polarization. These experiments will be carried out with use of two custom-made set-ups.

Chapter 2

Theory

Before the establishment of the microscope by Antony van Leeuwenhoek in 1673 [1], basically no one had had any knowledge of the world below the millimetre scale. The smallest living creature known in that time would be species of mite which, by microscope standards, still reaches a colossal size of 0.3 mm [2]. Since the Dutchman's discovery, many new scientific disciplines have emerged and great progress has been made in our understanding of the very small which, (in)directly, gave us further understanding of systems much larger than a mere mite. However, the smaller the matter we wish to study becomes, the harder it gets to overcome the many difficulties and limits that arise within light microscopy. Nevertheless, in the years more and more techniques and theories have been put forward which have enabled us to overcome certain limits and to reach new levels of control.

2.1 Light Microscopy

To understand the implications of using light microscopy, we will first discuss the basic properties of light. When Maxwell first used his theory to describe an electromagnetic wave in vacuum, he found that this wave must travel with a speed equal to the speed of light as had been measured in experiment. This observation led him to conclude that light must be a transverse electromagnetic wave with both an electric- and a magnetic component. Subsequently, he found that the electric field of a plane electromagnetic wave traveling in the $\hat{\mathbf{z}}$ direction, is given by:

$$\mathbf{E}(z, t) = \mathbf{E}_o e^{\frac{2\pi i}{\lambda}(z - vt)} \tag{2.1}$$

Where λ equals the wavelength of the wave and v is its velocity. Here, the amplitude of the wave, $\mathbf{E}_o$ is a vector and its direction is called the polarization of the wave while its magnitude is called the amplitude. Another important concept in wave physics is the concept of phase. The phase of a wave gives the fraction of the wave cycle that has elapsed relative to the origin. Here, we first define a state of the wave as the origin with phase 0. Then, moving further in space (or time) the phase will linearly increase from 0 to 2π where the state of the wave is equal to the state at the origin. To illustrate, this means that a position where the phase of the wave is π tells us the wave is halve way through its cycle. To summarize, the phase ϕ of the wave at a
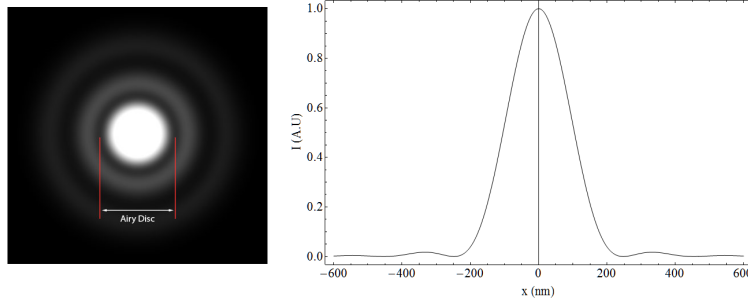
Figure 2.1: Computer simulation of the Airy Disc. The right profile plot shows the Airy Disc for a system where $r_{\text{Airy}} \approx 250$ nm. [4].

position z where the origin is at $z = 0$ is given by:

$$\delta\phi(z) = \frac{2\pi}{\lambda}(z \mod \lambda) \tag{2.2}$$

Finally, phase is used to compare the states of two waves with the same frequency v/λ to compare their relative states. If two waves are simultaneously in the same part of the cycle they are said to be 'in phase'.

Now, we will see that these wave-like properties of light limit the image resolution of a microscope: if an uniform bundle of light is focused, the lateral intensity distribution in the focus will have the shape of finite-sized spot with light/dark rings surrounding it, known as the Airy Disc [3]. This pattern is shown in figure 2.1. The (lateral) radius of the first dark ring surrounding the central spot can be shown to be:

$$r_{\text{Airy}} = 1.22\frac{f\lambda}{D} \tag{2.3}$$

Here, f is the focal length of the lens, λ is the wavelength of the light in vacuum and D is the diameter of the focused beam. In microscopy, a more common and useful way to describe the properties of the focus lens (objective) is by its Numerical Aperture (NA), defined as:

$$\text{NA} = n\sin\theta \tag{2.4}$$

where n the refractive index of the medium and θ is the halve angle at the focus spanned by the optical axis and the beam diameter, see figure 2.2. From this figure, it can easily be shown that the the NA of the objective and its other properties relate as follows:
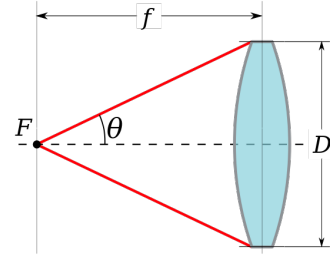

Figure 2.2: Schematic drawing to show how the Numerical Aperture (NA) of a lens is related to its other properties.

$$\text{NA} = n\sin\left(\arctan\frac{D}{2f}\right) \approx n\frac{D}{2f} \tag{2.5}$$

Where the last approximation is usually valid in the case of a microscope objective. Notice that the NA of a microscope not just tells us at which angle light is focused on the sample, but that this also describes the range of angles at which light can be collected from the sample, meaning objectives with a high NA are able to collect more signal. Subsequently, we now get for r_{Airy}:

$$r_{\text{Airy}} = 0.61\frac{\lambda}{\text{NA}} \tag{2.6}$$

This equation gives the spot size of a laser bundle given the wavelength λ of the bundle and the objective's Numerical Aperture. Clearly, a high NA results in a smaller focus spot. The relationship between spot size and resolution is an important one: this is illustrated for scanning microscopy where images are constructed by scanning a focus through a part of the sample while collecting signal at predetermined positions (pixels). This in contrast to wide-field microscopy where the entire sample is illuminated simultaneously. In the case of scanning microscopy, the finite size of the focus causes an object in the sample to be imaged as a convolution of the object with the focus. To understand this, assume one images a reflecting point particle $\delta(t, s)$ by scanning through it with a focus with intensity distribution $A(x, y)$. During the scan the focus will illuminate a finite area of the sample larger than one pixel. Then, whenever the particle is present somewhere inside the illuminated area, signal will be collected. Mathematically, we get:

$$I(x, y) = \iint \delta(t, s)A(x - t, y - s)dsdt = A(x, y) \tag{2.7}$$

such that this particle will be imaged as a spot with radius r_{Airy}. Additionally, if two (or more) small particles are separated by a distance smaller than $2 \cdot r_{\text{Airy}}$, the convolutions of the particles will overlap, see figure 2.3. Classically, if the spatial distance between the particles is in Smaller than r_{Airy}, the particles will appear merged and one is unable to resolve them, preventing the microscope to distinguish structures within this order of magnitude. Commonly, the minimum distance between resolvable particles is the definition of spatial resolution in microscopy. In this case, this distance is known as the Rayleigh Criterion which in equation form, results in equation 2.6. To put this limit in perspective, visible light has a wavelength in the order of the 10^2 nm

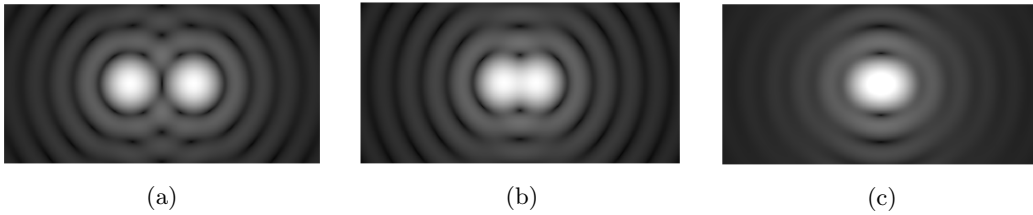(a)   (b)   (c)

Figure 2.3: Series of images illustrating the ability of a microscope to resolve individual particles: Fig. a, two convolved point particles with no overlap are resolvable. Fig. b, a convolution of two point particles with a small overlap can still be deconvolved. Fig. c, if the distance between the particles is too small, it is no longer possible to resolve the particles.

and practically, the highest NA possible for an air objective ($n = 1$) equals 0.95. As a result, a light microscope will have a resolution in the order of 10^2 nm. Unfortunately, many biological structures have sizes or posses details well below this resolution. As a result, conventional light microscopes will be unable to fully resolve these samples. Now, it is sometimes possible to deconvolve the image afterwards with a computer to obtain a higher resolution image [5]. However, deconvolution is often not possible if proper knowledge (particle size, background, noise, etc.) is unavailable nor practical since the computation cost is high [6].

2.1.1 Fluorescent Microscopy

In light microscopy, images are generally not (just) formed by collecting the reflection of the illumination light. Instead, more often a property of certain molecules and structures to fluoresce is used: this is the ability of particles to absorb photons within a certain energy range by excitation of an electron in its outer shell to a higher energy level.

After the electron has been excited it will lose some energy due to non-radiative processes before it falls back towards its original energy level by emission of a photon with a slightly lower energy (higher wavelength). This process is schematically illustrated in figure 2.4. Many (biological) structures exhibit fluorescent properties and even when they do not, it is possible to label them with fluorophores, as a very nice property of fluorescence microscopy is the fact that the emission spectrum is very molecule-specific, making it possible to recognize specific fluorophores in the sample by means of spectroscopy. Unfortunately, the Rayleigh Criterion

Figure 2.4: Jablonski diagram illustration the fluorescence process [7].

still holds true for fluorescent microscopy. Additionally, the process is destructive to the fluorophores such that after a number of fluorescent cycles, the fluorophore molecule will break down or 'bleach', which means signal can no longer be extracted from it. Still, fluorescent microscopy is very popular and it has seen many new applications and improvements over the years. One of the latter is a method to increase the image resolution beyond the Rayleigh Criterion, known as Stimulated Emission Depletion microscopy.

2.1.2 STED: increasing the resolution with doughnuts

The apparent hard limit that the Rayleigh Criterion prescribes, has not stopped scientists to develop methods that defy it. These methods are appropriately dubbed 'super resolution' techniques and one of these methods is the previously described subsequent deconvolution of microscope images to obtain a much better resolution. A different, increasingly popular method which works with fluorescent microscopy, is called Stimulated Emission Depletion (STED) microscopy. In contrast to deconvolution, STED will increase the resolution of the microscopy in 'real time' by decreasing the effective radius of the focus spot in the microscope. To achieve this, a STED set-up utilizes two lasers: the first provides the usual excitation spot like any

regular fluorescent microscope, pushing electrons in a higer energy level. The second however, will de-excitate (deplete) the outer part of the excitation spot such that an excitation spot is left with a much smaller radius. Figure 2.5 illustrates this process: after the excitation beam has illuminated the sample, it will leave a part of the sample excited (figure 2.5a). Afterwards, a doughnut shaped beam (2.5b) will deplete part of the just excited fluorophores. Due to the shape of this beam, mostly the center part of the illuminated area will be still be excited and provide signal (figure 2.5c). This way, two bundles both obeying Rayleigh Criterion can create a system with a much lower effective lateral resolution. Now, one might wonder what the resulting

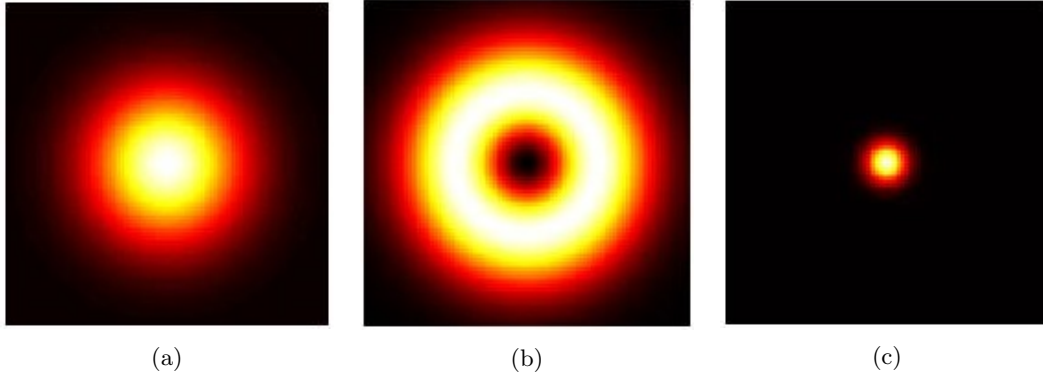(a)   (b)   (c)

Figure 2.5: Series of images shown to illustrate the STED process. fig. a shows the shape of the excitation spot after the laser has illuminated the sample. Next, fig. b shows the shape of the focus the depletion beam which will de-excite part of the excitation shop. Afterwards, the area in the sample which has been excited has been reduced in size significantly (fig. c).

resolution of a STED microscope is quantitatively. Unfortunately, this is not as trivial as one might assume, as the excitation spot that results from the two laser beams is not just dependent on the relative shapes, but also on the relative intensities of the bundles. However, the key is to determine the radius at which significant de-excitation is achieved. This radius is dependent on several properties such as:

- the radius of the doughnut of the depletion beam: obviously, if the radius of the doughnut is larger, the resolution becomes worse. Ideally, this radius is as small as possible.

- the intensity in the center of the depletion beam: if the intensity in the center of the depletion beam is not zero, it will decrease signal.

- the relative intensities of the two beams: the higher the relative intensity of the doughnut spot, the bigger the region where significant depletion is achieved, the better the resolution.

In practise, many factors will play a role on the quality of STED and resolutions between 80 nm to 2.5 nm have been reported [8]. Because of these reasons, it is very important to be able to correctly describe the doughnut shape of the depletion beam.. In this thesis, the generation and the characterization of STED doughnuts will be the key subject of study and we will focus our analysis on the first two points just mentioned.

2.2 Fourier Optics

To understand how we can obtain a doughnut shaped focus, we will now discuss a field of study named Fourier Optics which states that lenses in certain situations can perform a Fourier Transformation on a beam of light. With it, we can better understand how we are to modulate the focus from a spot to a doughnut. Here, we will only discuss this subject with a focus on its applications, as it is important to fully grasp its origin in order to use it.

2.2.1 The Fresnel Integral

Fourier Optics finds its origin in Christian Huygens who tried to explain the physical properties of light in a more elegant and powerful manner than the by then accepted ray optics: he (correctly) assumed that light is a type of wave and that every point on the wave front can be interpreted as an individual point source. A century later, Augustin Fresnel translated Huygens' theory to a mathematical model and even though the model had no basis in experiment, it was remarkable that Huygens' principle was found to agree quite well with experimental results. Later, other scientists such as Gustav Kirchhoff gave more theoretical derivations of the theory, confirming that Huygens' model was conspicuously accurate.

To explain how light propagates according to Fresnel-Huygens theory, we will introduce the following system: a light beam travels through the vacuum in the $\hat{\mathbf{z}}$-direction where we focus on the complex wave field $E(\xi, \eta)$ of this light in the (ξ,η) plane perpendicular to $\hat{\mathbf{z}}$. Next, we are interested in the complex wave field $E(x,y) = E_o(x,y)e^{i\phi(x,y)}$ in the (x,y) plane located a distance z from the (ξ,η) plane, see figure 2.6. Here, $E_o(x,y)$ is the amplitude of the electric field while $\phi(x,y)$ is the phase. Here, we will refer to the $E(\xi,\eta)$ as the Fourier plane and to $E(x,y)$ as the image plane. As mentioned earlier, the Huygens-Fresnel principle assumes that every point of $E(\xi,\eta)$ can be seen as its own point source and the final wave field $E(x,y)$ is the sum of all the contributions of these point sources. Additionally, Fresnel found that two corrections where needed to obtain agreement with his measurements. The first of which was a pre-factor i/λ and the second was a so-called obliquity factor which we have taken as $\cos\theta$. What resulted is now known as the Fresnel-Huygens Diffraction Integral [9] [10]:

Figure 2.6: Geometry of eq. 2.8 [9].

$$E(x,y) = \frac{i}{\lambda}\int_{\Sigma} E(\xi,\eta)\frac{\exp\left[ikr\right]}{r}\cos\theta ds \qquad (2.8)$$

Where r is the distance between points $P_1(\xi,\eta)$ and $P_o(x,y)$ and Σ describes the area of the cross section of the beam. At this time, it is found useful to convert the variables in the integral to Cartesian coordinates. From geometry in figure 2.6, it can be shown that that r equals:

$$r = z\sqrt{1 + \left(\frac{\xi - x}{z}\right)^2 + \left(\frac{\eta - y}{z}\right)^2} \qquad (2.9)$$
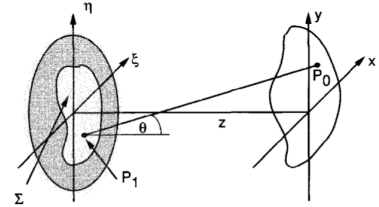
10

In many cases, z will be much larger than the (maximum)lateral distances $\xi - x$ or $\eta - y$ between two points. Therefore, we can approximate eq. 2.9 to the first order binomial expansion obtaining:

$$r \approx z \left[1 + \frac{1}{2} \left(\frac{\xi - x}{z} \right)^2 + \frac{1}{2} \left(\frac{\eta - y}{z} \right)^2 \right] \tag{2.10}$$

These results, combined with placing the finite size of the beam in the definition of $E(\xi, \eta)$, eq. 2.8 can shown to be approximately:

$$E(x, y) = \frac{ie^{ikz}}{\lambda z} e^{\frac{ik}{2z}(x^2 + y^2)} \iint_{-\infty}^{\infty} E'(\xi, \eta) e^{-\frac{1}{\lambda z} 2\pi i (\xi x + \eta y)} d\xi d\eta \tag{2.11}$$

with:

$$E'(\xi, \eta) = E(\xi, \eta) e^{\frac{ik}{2z}(\xi^2 + \eta^2)} \tag{2.12}$$

Here, you can recognize the integral as a Fourier Transform of $E'\left(\frac{\xi}{\lambda z}, \frac{\eta}{\lambda z} \right)$ which means that the field $E(x, y)$ (aside from some pre-factors) can be found by Fourier transforming the field of $E'\left(\frac{\xi}{\lambda z}, \frac{\eta}{\lambda z} \right)$ after it has been multiplied by a quadratic phase factor.

2.2.2 Fourier Lens

we will see that the Fourier Transform is approached even more accurately if a lens is placed between the two planes. We begin by describing the shape of the lens as a function of the distance from the optical axis. To illustrate this, a lens is schematically illustrated in figure 2.7.

Here, the lens is divided into three parts $01, 02$ and 03. The thickness of the total lens in the optical axis is Δ_o. If R_1 and R_2 are the radii of curvature of section 1 and 2 respectively, it follows from the geometry of fig 2.7 that the thickness $\Delta(\xi, \eta)$ of the lens, assuming a small radius of curvature, equals:

$$\Delta(\xi, \eta) = \Delta_o - \frac{\xi^2 + \eta^2}{2} \left(\frac{1}{R_1} - \frac{1}{R_2} \right) \tag{2.13}$$

Figure 2.7: Schematic illustration of a lens, where the radius of curvature R_2 of part 02 of the lens is shown.

Due to the refractive index n of the lens, light propagate more slowly in the lens than in the vacuum. As a result, the phase modulation of the light due to the lens depends on the thickness at the point of incidence:

$$\delta\phi(\xi, \eta) = kn\Delta(\xi, \eta) + k(\Delta_o - \Delta(\xi, \eta)) \tag{2.14}$$

Here, the first part of the equation gives the phase delay as a result of the lens, while the second part in the equation is the phase delay resulting from the remaining free space. Assuming a collimated, uniform beam with amplitude E_o, $E(\xi, \eta)$ directly after the lens is given by:

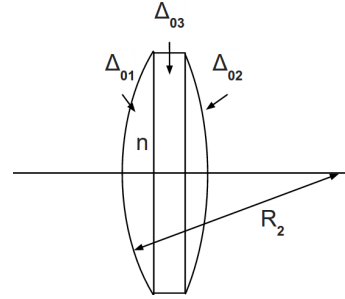$$E(\xi, \eta) = E_o e^{ik(n\Delta(\xi, \eta) + \Delta_o - \Delta(\xi, \eta))} \tag{2.15}$$

Now, we substitute the previously derived function for $\Delta(\xi, \eta)$:

$$E(\xi, \eta) = E_o e^{ink\Delta_o} e^{-\frac{ik}{2f}(\xi^2 + \eta^2)} \tag{2.16}$$

where we have combined the part of the formula containing the physical properties of the lens n, R_1 and R_2 in a single value f, called the focal length of the lens:

$$\frac{1}{f} = (n - 1)\left(\frac{1}{R_1} - \frac{1}{R_2}\right) \tag{2.17}$$

we can conclude that a lens will introduce a circular quadratic phase shift to a wave front which can be mathematically expressed as:

$$T_l = e^{-\frac{ik}{2f}(\xi^2 + \eta^2)} \tag{2.18}$$

where we have dropped the constant phase term, since only the relative phase is interesting. Therefore, a lens will introduce the phase shift found in eq. 2.18. As a result, the part of eq. 2.11 within the integral for a system with a lens becomes:

$$\iint_{-\infty}^{\infty} E'(\xi, \eta) T_l e^{-\frac{1}{\lambda z} 2\pi i(\xi x + \eta y)} d\xi d\eta \tag{2.19}$$

If we now work out the functions within this Fourier integral, we get:

$$E'(\xi, \eta) T_l = U T_l e^{\frac{ik}{2z}(\xi^2 + \eta^2)} = U e^{\frac{ik}{2}(\frac{1}{z} - \frac{1}{f})(\xi^2 + \eta^2)} \tag{2.20}$$

Such that in the case of $z = f$, we end up with:

$$E'(\xi, \eta) = E(\xi, \eta) \tag{2.21}$$

Which means that the integral in eq. 2.11 becomes a true Fourier integral and only the Fresnel term outside the integral remains. To recall, z was the distance between the two planes in figure 2.6: apparently, if an image plane is placed directly against the lens, the Fourier transform of the image should be found in the focal plane of the lens. This is the fundamental understanding that has led to the discipline of Fourier Optics. Additionally, one can show that the Fresnel term outside the integral disappears in case the (ξ, η) plane is also placed a distance f in front of the lens, which means that $E(x, y)$ will be the exact Fourier transform of $U\left(\frac{\xi}{\lambda f}, \frac{\eta}{\lambda f}\right)$. we will use these observations to explain the effects of beam modulation on the shape of the focus by the Spatial light modulation.

2.3 Doughnut beam generation

Now, we will use the previous to discuss how the doughnut is generated in STED microscopy. To start, we will first describe in more detail how the intensity distribution in a focus is calculated for a regular, uniform bundle. Then, we will show how one can modulate the beam such that instead of an Airy Pattern, a Doughnut shaped focus will form. To explain this, we will look now at the diffraction of light that occurs in the case of a circular aperture, as illustrated in figure 2.8, which shows the geometry of the situation. Here, light enters an aperture with radius a from the left side behind the blue surface. Subsequently, the intensity distribution that appears on a surface a distance L from the aperture can be calculated. As we have already seen, the electric field amplitude $E(q, \varphi)$ in the far-field due to diffraction at the circular aperture can be calculated by a Fourier Transform. If we convert eq. 2.11 to cylindrical coordinates, it can be shown that [11]:
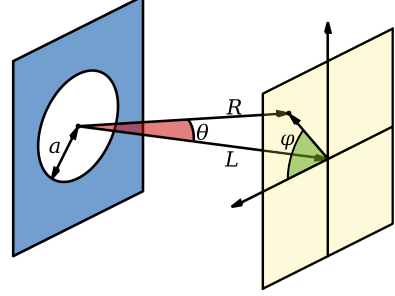

Figure 2.8: Geometry of diffraction with a circular aperture. Not shown are the cylindrical coordinates in the aperture plane Φ and ρ.

$$E(q, \varphi) \propto \frac{1}{L} \int_{\rho=0}^{a} \int_{\Phi=0}^{2\pi} E(\rho, \Phi) e^{i(k\rho q/L)\cos(\varphi-\Phi)} \rho d\rho d\Phi$$

(2.22)

Again, this equation tells us that the (complex) electric field at a position in the far field is proportional to the sum of all the contribution of the different rays of light at the aperture, taking into account possible interference between the different rays. In the case of an uniform, coherent bundle with unit intensity, we get $E(\rho, \Phi) = 1.0$. Additionally, in this case we expect rotational symmetry in the far field which means we can take $\varphi = 0$. Subsequently, the integral becomes:

$$\int_{\rho=0}^{a} \int_{\Phi=0}^{2\pi} e^{i\frac{k\rho q}{L}\cos\Phi} \rho d\rho d\Phi$$

(2.23)

where the inner integral has the same form as the zero-th order Bessel Function $J_o(u)$ with $u = k\rho q/L$, which can be defined as [12]:

$$J_o(u) = \frac{1}{2\pi} \int_0^{2\pi} e^{u\cos\nu} d\nu$$

(2.24)

Subsequently, we can write:

$$E \propto \frac{2\pi L}{(kq)^2} \int_{u=0}^{u=kaq/L} J_o(u) u \, du = 2\frac{\pi a^2}{L} \frac{J_1(kaq/L)}{kaq/L}$$

(2.25)

where we have used the following identity of the J_o:

$$\int_0^w J_o(u) u \, du = w J_1(w)$$

(2.26)

Finally, by placing a lens with focal distance f in the circular aperture, such that the just derived intensity distribution will exist in the focus of the lens, it can be shown that for $I(q)$ in the case of an uniform, coherent bundle through a circular aperture we get in the focus f:

$$I(q) = I_o \left[2 \frac{J_1(kaq/f)}{(kaq/f)} \right]^2 \tag{2.27}$$

where we have used the fact that for the (average) intensity holds $I = 0.5EE^*$ (or $|E|^2$). This is the function of an Airy Disc with center intensity I_o, and it is the function visualized in figure 2.1. Additionally, in the case of microscopy, it is more useful to express $I(q)$ in terms of experimental properties like NA and λ. This way, we get:

$$I(q) = I_o \left[2 \frac{J_1(\frac{2\pi \text{NA}}{\lambda} q)}{\left(\frac{2\pi \text{NA}}{\lambda} q \right)} \right]^2 \tag{2.28}$$

Clearly, the size of the focus spot of an objective is determined by the NA of the objective and the wavelength of the laser, as we have seen before in eq. 2.6. Now, how do we go from a Airy pattern to a doughnut? Frankly, this is surprisingly simple: we keep the same geometry and uniform bundle. However, this time we take the uniform beam and assume it has a phase that linearly changes with the angle Φ such that we get:

$$E(\Phi) = 1.0 e^{i\Phi n} \tag{2.29}$$

This phase distribution is often called a vortex and n is the topological charge of the vortex. To clarify the shape of the phase distribution, figure 2.9a shows a two-dimensional representation of the phase with a phase mask for $n = 1$: it shows a cross section of the beam in grey scale where phase is represented from 0 (black) to 2π (white). Obviously, the position of the 0 is arbitrary as the phase of a wave only has meaning if it is compared to the phase of a different part of the beam. Furthermore, since 0 and 2π mean equal phase, the two extremes in the image represent equal phase. Finally, figure 2.9b shows the phase using a three-dimensional image for more clarity: the phase has the shape of a corkscrew. It is noteworthy, that near the center of the beam, light of all phases is present. This will lead to destructive interference which can make it insightful why the center will show a minimum for this beam, as we shall see. At this point, we again use in eq. 2.29 to calculate the intensity distribution in the focus:

$$E(q, \varphi) \propto \frac{1}{L} \int_{\rho=0}^{a} \int_{\Phi=0}^{2\pi} e^{i(\Phi n + \frac{k\rho q}{R} \cos(\Phi))} \rho d\rho d\Phi \tag{2.30}$$

This time, if we take $n = 1$ the part in the integral has the same form as the *first* order Bessel Function $J_1(u)$ with $u = k\rho q/L$, which can be defined as:

$$J_1(u) = \frac{1}{2\pi i} \int_0^{2\pi} e^{i(\nu + u \cos(\nu))} d\nu \tag{2.31}$$

Subsequently, we now use the following approximation [14]:

$$\int_0^u J_1(w)w dw = \frac{\pi}{2} u \left[J_1(u) H_o(u) - J_o(u) H_1(u) \right] \tag{2.32}$$
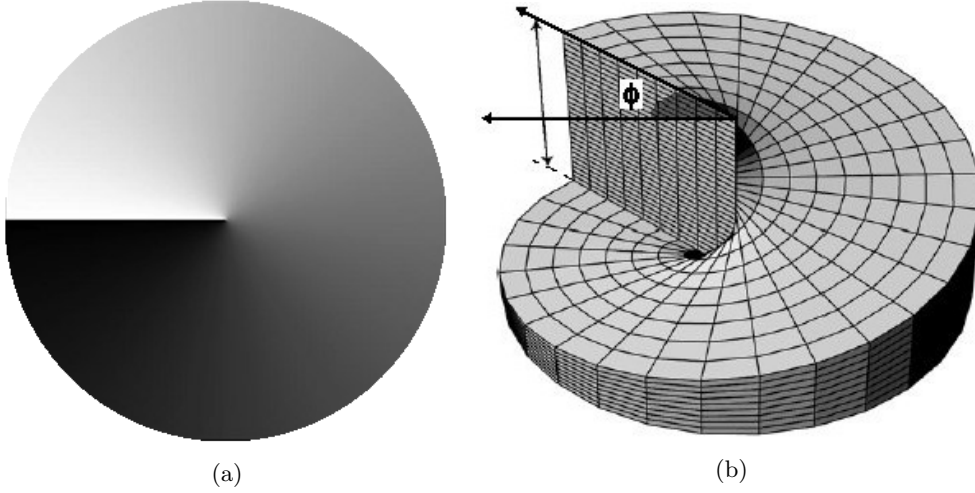
14

(a)   (b)

Figure 2.9: Two images showing the phase distribution of the cross section of the beam, expressed by equation 2.29. The right image is taken from Leach *et al.* (2004) [13].

where H_o and H_1 are respectively known as the first- and second order Struve functions. Then, this will give for the intensity in the case of a lens placed in the aperture:

$$I(q) = I_o \left[\pi \frac{J_1\left(\frac{2\pi \mathrm{NA}}{\lambda}\right)H_o\left(\frac{2\pi \mathrm{NA}}{\lambda}\right) - J_o\left(\frac{2\pi \mathrm{NA}}{\lambda}\right)H_1\left(\frac{2\pi \mathrm{NA}}{\lambda}\right)}{\frac{2\pi \mathrm{NA}}{\lambda}} \right]^2 \tag{2.33}$$

This result is visualized in figure 2.10 where 2.10a shows the the result from equation 2.33 compared to the Airy Disc (dashed) for the same I_o. From this figure, it can be seen that we expect zero intensity in the center, as was desired. Not surprisingly, the doughnut has a lower peak intensity as the total power contained in the focus must be conserved. For completeness, a graph which compares the approximation made in eq. 2.32 to the exact (numerical) solution of the integral is shown in figure 2.10b which shows that the made approximation is very accurate. Before we continue, one might wonder what the effect of a higher topological charge n will be on the doughnut shape is, as it makes sense that this will give an even more effective vortex. However, higher values of n will result in an increase of the doughnut focus size, making them unpractical for STED microscopy. Additionally, it must be noted that a negative topological charge ($n = -1$) will mirror the direction of the phase delay which will, in this case, give the same focus shape. In experimental set-up, the required phase distribution is often obtained using a vortex phase plate, generating the phase required for the STED doughnut. These optical elements can create nearly perfect vortexes. However, they are very inflexible as they only work for specific wavelengths. As mentioned in the introduction, we will try to generate doughnuts using a Spatial Light Modulator (SLM) instead, which is technically a variable phase plate, such that we're able to control the phase distribution of the light. As a result, a SLM is more versatile and should be able to successfully modulate light of multiple wavelengths as well as correct set-up misalignment. For these reasons, a SLM is interesting to study. In chapter 3, we will discuss the properties of the Spatial Light Modulator in greater detail.
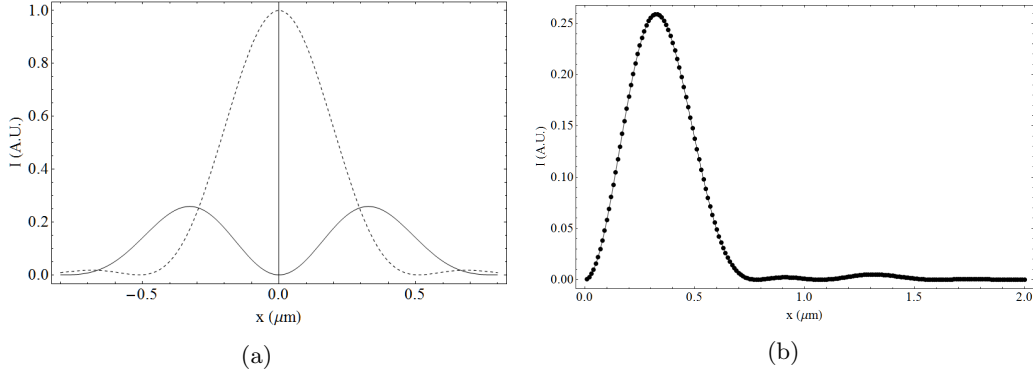
15

(a)   (b)

Figure 2.10: Fig. a shows the intensity profiles in case of a circular aperture and an uniform bundle for both an uniform phase- (Airy Disc, dashed) and a vortex phase bundle (Doughnut, solid). Fig. b compares both sides of eq. 2.32 where the left side has been calculated numerically.

Finally, we can conclude that a beam with a vortex phase will have a focus in the shape of a doughnut. Additionally, it can be shown that this still holds true if a Gaussian beam is assumed instead of an uniform bundle. In future characterization of the doughnuts, we will not always use the approximation of eq. 2.32 as we do not have an uniform beam. In that case, we will evaluate the integral numerically.

2.4 Polarization: doughnuts and high NA

So far, our calculations have neglected the polarization of the light. In fact, the diffraction integral used previously only takes amplitudes into account assuming all parts of the beam interfere freely, which is not necessarily the case. Usually, light from a laser is linearly polarized and
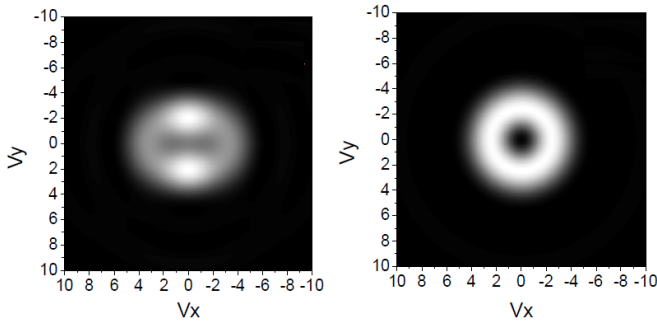
Figure 2.11: The calculated focus shapes of linearly polarized light in the V_x direction, obtained using an objective with NA of 1.0 (left) and 0.2 (right), taking into account depolarization effects. Image taken from Ganic *et al.* (2003) [15].

the calculations hold up fine. However, lenses, especially objectives with a high NA, exhibit a depolarization effect [16] and as a result, we can not just assume our current predictions to hold up in these cases. Therefore, we need to take a look at the effect of polarization on the shape of the doughnut in focus. Fortunately, research on this topic has already be conducted which we will discuss here. Figure 2.11 shows some results obtained from computer simulations taken

from Ganic *et al.* (2003) [15]. The right image is the result of a simulation for linearly polarized light in the V_x direction in the case of an objective with a NA of 0.2. Apparently, our previous calculations hold up quite well in this case as it shows the predicted symmetric doughnut with a nice minimum in its center. However, if we shift our focus towards the left image, which assumed a very high NA of 1.0; it shows grave distortion of the doughnut: not only has the rotational symmetry disappeared, showing increased relative intensity in the V_y direction. Additionally, the center minimum is non-zero and elongated which, as we discussed, has a large effect on the quality of STED.

Where does this distortion originate? Interestingly, it was found that the effects of the objective introduce a V_z (axial) component of the electric field in the focus which in the case of a vortex phase has its maximum in the center of the focus, causing the increased minimum seen in the upper part of figure 2.11. Besides, even though the V_x component still has the shape of a doughnut, it has lost its rotational symmetry forming the observed aberrations. From the
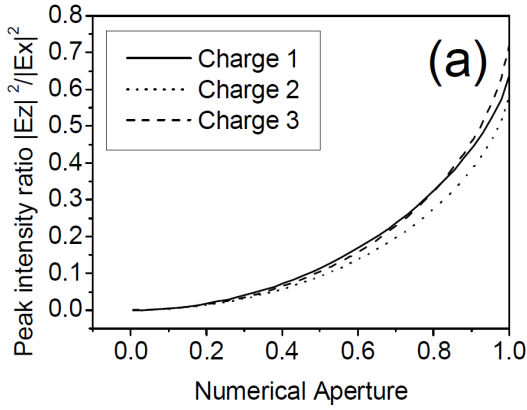

Figure 2.12: The calculated ratio of $|E_z|^2/|E_x|^2$ as a function of NA, giving an indication on the distortion caused by the depolarization in the objective. The figure has plotted results for three different values of topological charge. As mentioned earlier, we are only interested in a charge of '1', while other charges seem to behave similarly. Image taken from Ganic *et al.* (2003) [15].

paper, it was observed that the V_z component has its intensity nearly completely centralized in the center, while the V_x component still possess a nice center minimum. Therefore, the ratio $|E_z|^2/|E_x|^2$ can give us some information on the quality of the minimum in the center, indirectly quantifying the deviation from the 'perfect' doughnut shape. This ratio is plotted as a function of NA in figure 2.12, taken from the same paper. Here, we indeed see an increase of the ratio $|E_z|^2/|E_x|^2$ for larger NA. Interestingly, the ratio seems to be rather small for low NA (< 0.4) but it rapidly increases after a NA of approximately 0.5, showing that the polarization will have a large impact on the shape of the focus. Note that in these calculations, n was assumed unity so that we get $NA = \sin\theta$. While the implication of figures 2.11 and 2.12 do not seem very encouraging, it is still possible to obtain an undisturbed doughnut in the focus as similar calculations have shown nice results in the case of circularly polarized light [17]. Figure 2.13, shows these calculations. Here, it is also shown that the orientation of the circularly polarized light is very important as it has to be the same as the orientation of the vortex phase: else the results show a worse minimum than linearly polarized light, despite the nice angular symmetry. In this case, it must be noted that instead of altering the direction of the polarization, it is
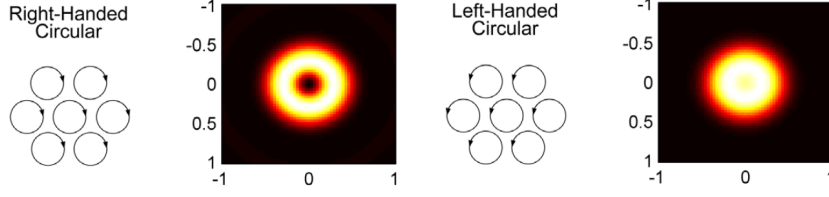
Figure 2.13: The direction of the circular polarization compared to the direction of the vortex phase has a big effect on the quality of the zero. Image taken from Hao *et al.* (2010) [17].

also possible to change the direction of the phase by changing the sign of the topological charge n.

To summarize, we expect polarization to play a big role in the shape of the doughnut for objective with a high Numerical Aperture. Since these doughnuts are utilized in STED microscopy, practically all relevant experimental set-ups will contain these objectives, since they are necessary to increase the resolution of the microscope. Therefore, for complete characterization, it is important to take into account the polarization in the experiment.

2.5 Gerchberg-Saxton Algorithm

Lastly, to show a relevant application of Fourier Optics and to give more insight in the capabilities of a SLM, we will now briefly discuss a famous algorithm which applies this theory. let's say we desire an intensity distribution $I_1(x, y)$ which is much more complex than, for example, a doughnut and we wish to know if we there is a phase mask that will generate this shape if a bundle of light is focused with this modulated phase. In this problem, the two electric field amplitudes are known (the initial distribution $|E_o|$ and the desired distribution $|E_1| = \sqrt{I_1}$), the initial phase $\phi_o(\xi, \eta)$ is the to be determined variable (the phase mask) while $\phi(x, y)$ is a free parameter because for now we are not interested in the phase at the focus, just the intensity. This problem of finding $\phi_o(\xi, \eta)$ is known in literature as one variant of the *phase-retrieval problem*. If we now assume the observation of the previous section regarding the Fourier relation between the two planes to hold, we have the following relation between the parameters:

$$\mathcal{F}\left(|E_o(\xi, \eta)|e^{i\phi_o(\xi, \eta)}\right) = \sqrt{I_1(x, y)}e^{i\phi_1(x, y)} \qquad (2.34)$$

From this point we will for clarity, where possible, not show the variables of the amplitude and phase functions. The just described problem has been around for quite a while now and the most famous approach was published in 1972 by R.W. Gerchberg en W.O. Saxton. They introduced an iterative algorithm to recover ϕ_o for the given intensity pair E_o and E_1. This algorithm is now befittingly known as the Gerchberg-Saxton (GS) algorithm and it works a follows [18]:

- the algorithm starts by taking the of the complex electric field $E_o = |E_o|e^{i\phi_o}$ which contains the known source intensity $\sqrt{I_o} = |E_o|$ and a random ϕ_o.

- the (discrete) two dimensional Fourier transform of E_o is performed, resulting in E_1'.

- the phase of E_1', ϕ_1' is preserved, but the amplitude $|E_1'|$ is discarded and replaced with the square root of the desired intensity I_1, such that $E_1' = \sqrt{I_1}e^{i\phi_1}$

- the inverse Fourier transform of E_1' is performed, obtaining E_o'.

- finally, ϕ_o' of E_o' is preserved while the amplitude is now set to the square root of I_o, obtaining $E = |E_o|e^{i\phi_o'}$ which will be the input for the next cycle.

The idea is that $|E_1'|$ and $|E_1|$ will become more and more similar as more iterations are performed, which will mean that ϕ_o is the desired phase mask. For clarity, a diagram of the GS algorithm is shown in figure 2.14. Usually, the algorithm is stopped when the just mentioned
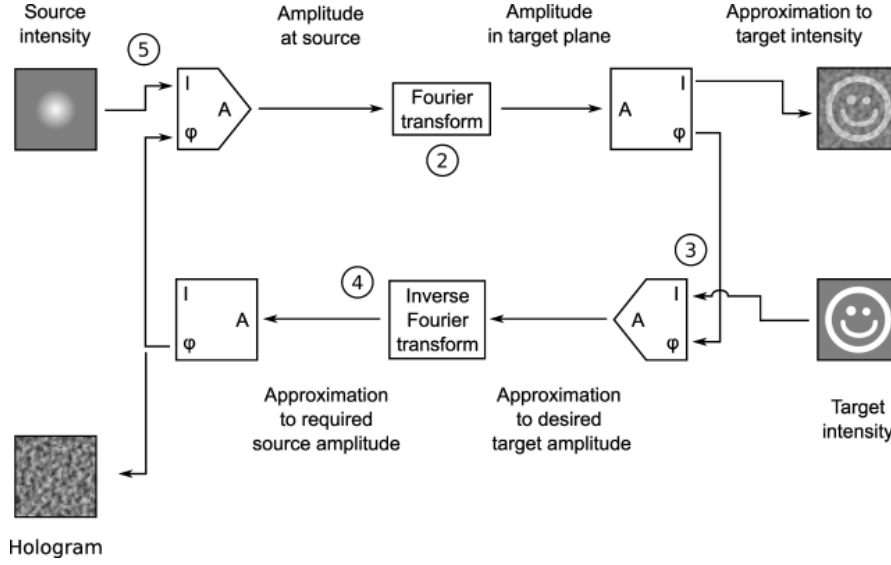

Figure 2.14: Diagram illustration the GS algorithm. Starting with the Fourier Transform of the source intensity I_s combined with a random phase ϕ_o, one discards the amplitude in the Fourier Domain and replaces it with the desired amplitude $|E_f|$. Afterwards, the Inverse Fourier Transform results in E_o' from which the phase ϕ_o' is used as the new input together with I_s.

parameters differ less than a certain threshold δ:

$$\sum |E_1'| - |E_f| < \delta \tag{2.35}$$

As is indicated in the example of figure 2.14, the GS algorithm should be able to produce foci in very unusual shapes like houses, faces, smiles, etc. which has found application in holography. Conclusively, if we can control the phase of a bundle, the algorithm can make it possible to use this to direct the shape of the beam in the focus. In this thesis, this will not be the focus of experiment, but we will try to use the Gerchberg Saxton algorithm to modulate the focus to arbitrary shapes and briefly report the results for further research.

Chapter 3

Instrumentation

To characterize the doughnuts we have split the experiment roughly in of two parts: firstly, we have continued previously performed research on the effects of the Spatial Light Modulator on light [19]. Secondly, we have researched the shape of SLM-generated doughnuts in a STED environment. Additionally, both parts have been researched using two different experimental set-ups and (re)building the set-ups was a large part of this thesis. Additionally, we will discuss some of the characteristics of the set-up like the effects of the spatial light modulator and give details about the performed measurements.

3.1 SLM set-up

The first set-up was centered around the SLM, and images were made directly of the SLM-modulated beam. Figure 3.1 shows the schematic outline of the set-up: an Omicron LuxX® 642 nm laser was used as a source of vertically polarized, coherent light. The radius of the beam was expanded by a beam expander with a 50 μm pinhole in its focus, generating a clean Airy Pattern which in laser physics is often approximated as a Gaussian Bundle. Then, the light falls on the SLM where it is modulated. Afterwards, the modulated light passes through a series of 20 cm lenses set up to form a 4f correlator, which will be discussed shortly. Finally, the beam is focused on a 1600x1200 pixel camera (Nikon Digital-Sight® 2MBWc, 1/1.8 inch, long axis: 7.2 mm) by a $f = 40$ cm lens. Importantly, because a lens is used to focus, we expect depolarization effects to be negligible. This way, we should be able to observe purely the effects of the SLM on the focus. This set-up was made for this thesis and no component was kept from the previous experiment [19].

From figure 3.1, it is clear the SLM is tilted slightly. Initially, this was not the case such that the modulated beam would travel back towards the laser. Because of this, a beam splitter was placed in this path in order to reflect (part of) the modulated light. Theoretically, this is a better way to set-up the SLM as currently light falls on the SLM at an angle which might cause small aberrations. However, it was found that the initial geometry showed fringing in the intensity pattern of the modulated light, possibly caused by interactions between the incoming
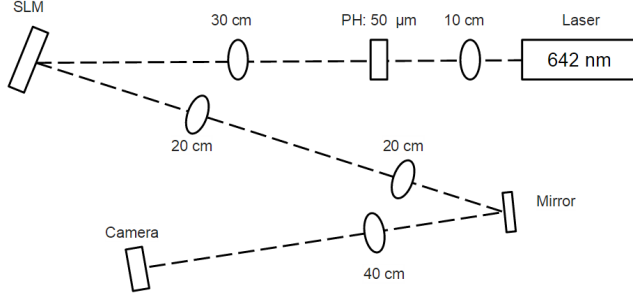
Figure 3.1: Schematic of the SLM setup: laser emitted light is expanded and cleaned up by a beam expander, before it falls on the SLM. After the beam is modulated by the SLM, it continues through a set of lenses before being focused in a camera, such that the shape of the beam in focus can be determined.

and outgoing light at the surface of the beam splitter. Additionally, the SLM was controlled by custom software written in LABVIEW. This software was partly rewritten as it contained some bugs, superfluous code and was not always user-friendly.

3.1.1   The Spatial Light Modulator

The Spatial Light Modulator that we have used was a Hamamatsu Liquid Crystal on Silicon (LCOS) SLM [20]. Its active area consisted of an LCD display containing 600x792 8-bit pixels with a short axis of 7.5 mm. Every pixel could be given a digital value from 0 to 255 which corresponds a phase delay it gives to the part of the light beam that falls on that particular pixel, such that the SLM should be able to give, to an extend, any arbitrary phase pattern to a beam of light. For example, one can generate a vortex phase by converting the values of the phase mask of figure 2.9a to the corresponding pixel values of the SLM. A phase mask where the phase values have been converted to the corresponding SLM pixel values is called a kinoform. After the light has passed through the SLM, its path continues as if the light has been reflected. If the SLM is connected to a computer, the PC would see it as an external monitor which made it very easy to display kinoforms on the SLM display.

When using spatial light modulators of this type, a few things are important to note. Firstly, the SLM will only effectively modulate light that is polarized in the direction of the orientation of the liquid crystals which, for the SLM setup, meant light had to be polarized in the vertical direction. Fortunately, this is the same polarization as the laser emits and no adjustments needed to be made. Secondly, even if the light is correctly polarized, the SLM will not be 100% efficient which means that part of the beam will remain its initial phase. This part of the beam we will dub the 'zero-th order' or 'reflected beam' as this part of the bundle is simply reflected at the SLM surface without modulation. The modulated beam we will call the 'first-order'. Thirdly, the pixel value that corresponds to a full 2π phase delay depends on the wavelength of the incident light, as the SLM in question is able to modulate light in the wavelength interval of 620-1100 nm. In the case of 642 nm, the 2π value was 127, which mend that the possible phase values given at every pixel are $n\pi/127$ with n an integer. Consequently, this means that at this wavelength the precision by which the SLM can introduce phase at every pixel is reduced by a factor '2' as the maximum number of possible values the SLM can display was 255. This is a downside of the

SLM: its window has a discrete grid and can only display distinct values and as a result the SLM will always approximate theoretical kinoforms to a certain extend. This could cause problems in certain situations.

Unsurprisingly, the fact that the SLM has such a control of phase, means it has far more capabilities than just creating vortexes. As we have seen, Fourier Optics implies that, under certain conditions, lenses can perform Fourier Transformations of the complex Electric Field at a particular wave front. On the other hand, we just described the SLM as controlling $\phi(\xi, \eta)$ and we have already seen that in that case we might be able to modulate the beam completely by displaying $\phi(\xi, \eta)$ resulting from the Gerchberg Saxton algorithm which mean we can, theoretically, approximate any desired focus. Because of this, SLM's like these and others have found (possible future) applications in many area's such as particle trapping [21], adaptive optics [22] and holography [23].

3.1.2 The 4f correlator

As mentioned before, the two lenses with a focal length of 20 cm form a 4f correlator. The 4f system is a widely used optical system, despite being a remarkably simple system; consisting of two lenses of equal focal length f. These lenses are placed $2f$ apart, as can be seen in the example of figure 3.2: if a wave front, in our case the SLM, is placed a distance f in front of one lenses,

the lens will perform a Fourier Transform of the wave front in the SLM plane, imaging it in the focus. Afterwards, this image will again be Fourier transformed, this time by the second lens, recreating the wave front of the object a distance f from the second lens. Now, the fact that the wave front of the beam in front of the 4f system is translated spatially, means that any small aberrations like deviations from the optical axis, are not present a that point. Moreover, the 4f correlator makes it possible

Figure 3.2: Schematic illustration of a 4f correlator.

place the wave front at the SLM 'inside' the objective lens by placing the lens a distance f from the second lens. This way, the Fourier Transform of the wave front should be imaged in the camera. Additionally, the mid-focus that appears between the two lenses makes it possible to block out-of-focus elements of the beam. For these reasons, we decided to also use a 4f correlator in the SLM set-up.

3.1.3 Beam modulation by the SLM

To gain more insight in the way a spatial light modulator modulates light beams and to take the first steps in characterizing its effects, we will now discuss to types of modulation that are very common. Firstly, it is possible for a SLM to change the beam direction. As a result the

beam will have a focus that is tilted laterally compared to the reflected beam. To obtain a tilt in, for example, the $\hat{\mathbf{x}}$-direction, the following phase modulation needs to be applied by the SLM window:

$$\delta\phi(x,y) = (2\pi na)x \tag{3.1}$$

Which basically is a linear relation between x and $\delta\phi(x,y)$ Here, n is the variable used to control the amount of tilt and a is a coefficient such that n corresponds to one $\delta\phi(d) = 2\pi n$ where d is the SLM window size in the direction of $\hat{\mathbf{x}}$. This way $n = 1$ corresponds to a single 2π cycle of phase shift between the two sides of the SLM. Figure 3.3a shows an example of a kinoform with $n = 8$ which can be placed on the SLM. Additionally, figure 3.3b explains the effects of the

Figure 3.3: Two images clarifying how tilt is generated.

(a) phase mask that will cause a tilt in the direction of the beam of light.
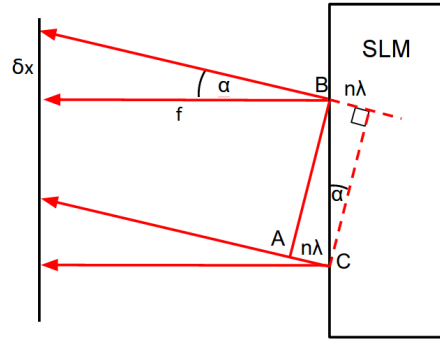
(b) Illustration of the effect of linear tilt on the SLM. If points A and C are $2\pi n$ 'out of phase', points A and B will form a new wave front.

phase mask on the beam: a linearly increasing delay of phase results in a tilt of the wave front of the modulated beam. Due to this tilt, the modulated beam diverges linearly from the zero-th order after leaving the SLM. From the figure, it can be shown that the expected lateral shift δx in the focus, in case of a 4f correlator, which puts the SLM wave front 'inside' the imaging lens, should be the equal to:

$$\delta x = f \cdot \tan\left(\arcsin\frac{n\lambda}{d}\right) \tag{3.2}$$

Where f is the focal length of the objective lens and λ equals the wavelength of the light. Since λ is very small compared to d, equation 3.2 can be approximated by:

$$\delta x = n\left(\frac{f\lambda}{d}\right) \tag{3.3}$$

Which means a linear relation can be expected between n and δx. This way the physical quantity δx has been related to the controllable quantity n in the program. To confirm this, δx was measured on the camera for increasing n and the results can be found in figure 3.4. Here, a

linear fit of the data is plotted in red. Besides the fit, equation 3.2 is shown (dashed), with the earlier mentioned values for all the instrumental constants. During this measurement, we could observe the effects of tilt on the camera where we estimate a typical error of ± 0.03 mm. This plot shows clearly that in this case, there is a good understanding of the effect of the SLM on the beam shape. Interestingly, we could have also predicted the tilt using Fourier Optics. For
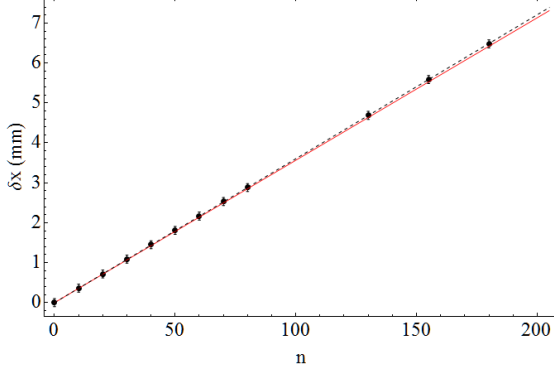

Figure 3.4: Figure showing the measured relation between n and δx. The dashed black line shows the linear fit of the data, while the red line show the graph of equation 3.2

this purpose, it is important to focus for a moment on the meaning of the coordinates in eq. 2.11: in this integral, the two set of coordinates were $\frac{x}{\lambda f}, \frac{y}{\lambda f}$ and ξ, η (for $z = f$). Since x, y are spatial coordinates, the latter pair of coordinates has the have the dimensions of m^{-1} and which is a frequency. In this case we interpret this as the frequency of the phase delay on the SLM or ϕ_o. Following this, we can see the tilt phase mask as a sawtooth function, see fig 3.5a. The Fourier Transform of this function is a series of equally spaced delta-functions with decreasing amplitudes representing the frequencies. Then, the primarily frequency F of the phase mask
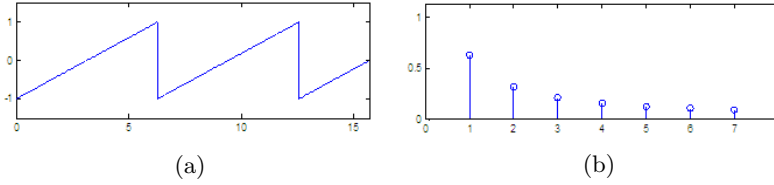
Figure 3.5: The sawtooth function and its Fourier Transform.

(the first harmonic) equals the number of sawtooths present per meter, or:

$$F = \frac{n}{d} \tag{3.4}$$

Then, the distance δx from the zero-th order this frequency will exist, equals:

$$F = \frac{n}{d} = \frac{\delta x}{\lambda f} \rightarrow \delta x = n\left(\frac{f\lambda}{d}\right) \tag{3.5}$$

Which is the exact position as predicted using ray optics. This suggests that for every frequency component in the phase mask, we expect an intensity spot in the focus. Finally, notice that the way the frequency is defined, it can also be interpreted as the slope of $\phi_o/2\pi$.

Next, similar measurements were performed for the kinoform generating an axial shift (defocus). In this case, the phase function is the shape of a two-dimensional, spherical parabola which causes the beam either to diverge or to converge. As a result, the focus is shifted in the axial direction. This time, the quantity n correspondents to the coëfficient in the parabola on the SLM window:

$$\delta\phi(x,y) = 2\pi n \cdot a(x^2 + y^2) \tag{3.6}$$

Notice that this follows directly from eq. 2.18. Here, a is again a pre-factor such that $\delta\phi = 2\pi n$ at the short edge of the SLM display ($x^2 + y^2 = 0.25d^2$). This means for a:

$$a = \frac{4}{d^2} \tag{3.7}$$

And, consequently:

$$\delta\phi(x,y) = \frac{8\pi n}{d^2}(x^2 + y^2) \tag{3.8}$$

The result form the previously calculated phase shift introduced by a lens was (eq. 2.18):

$$\delta\phi(x,y) = \frac{\pi}{\lambda f}(x^2 + y^2) \tag{3.9}$$

Comparing the two equations, can see $n < 0$ corresponds to a positive lens, such that the phase delay decreases radially. With the relation between $\delta\phi$ and f, it is possible to determine f_{SLM}, the focal length of the SLM, when this phase mask is applied:

$$f_{\text{SLM}} = \frac{d^2}{8\lambda n} \tag{3.10}$$

Finally, figure 3.6 illustrates the effects of the kinoform on the position of the focus. Assuming
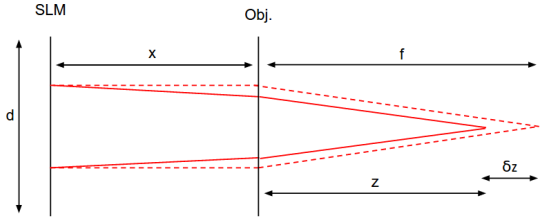
Figure 3.6: Illustration of the effect of a quadratic phase function on the axial position of the focus. In the case of a $4f$ correlator, $x = 0$ as in that case, the SLM window is imaged unto the objective lens.

the incident light is collimated and in the case of a $4f$ system, it can be shown using the lens formula, that the axial displacement δz as a function of n equals:

$$\delta z = \frac{1}{\frac{1}{f} - \frac{8\lambda n}{d^2}} - f \tag{3.11}$$

Where f is the focal length of the imaging lens. This time, we have measured $z = -(\delta z - f)$ as a function of n and the results are shown in figure 3.7, showing good agreement with the theoretical prediction. Here, the measurements were a little harder to perform as it was more

Figure 3.7: Figure showing the results from the measurements characterizing the effects of a defocus phase mask on the lateral position of the focus. Recall that $f = 40$ cm for the SLM setup. Again, the dashed line shows the predicted behaviour while the red line is the fit of the data.

difficult to accurately measure the distance from the focus point to the imaging lens, which results in the larger error bars. Still, the measurements again seem to agree very well w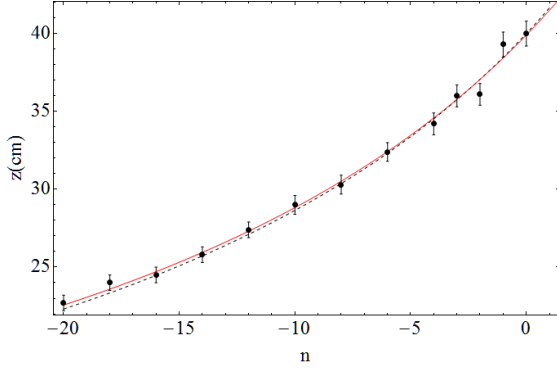ith the predicted curve. To summarize, the models introduced in theory are capable to predict the effects on the beam for the more simple phase masks. While these observations might seem not that useful, in fact they are quite significant if we wish to use the SLM for adaptive optics in the future. For example, it is possible to use the defocus to correct the beam if the sample is slightly out of focus. However, this means you need to be able to convert the n coefficient in the program to a physical shift δz in the focus. By confirming the models, the relation between n and δz is determined which makes it possible to use the SLM for these simple corrections.

Finally, we wish to note that it is possible to generate multiple modulations for a spot by simply summing over the individual phase masks. The kinoform $K(\xi, \eta)$ that needs to be displayed on the SLM to give the beam two or more phasemasks ϕ_n, is:

$$K(\xi, \eta) = \frac{n_{max}}{2\pi} \cdot \left[\left(\sum_{n=1}^{N} \phi_1(\xi, \eta) \right) \mod 2\pi \right] \tag{3.12}$$

where n_{max} is the value on the SLM LCD that corresponds to 2π. Additionally, in some applications, it is desired to obtain multiple, modulated beams. In this case, it can be shown the required kinoform can be found by calculating the complex argument of the array of the individual phase masks [24]:

$$K(\xi, \eta) = \frac{n_{max}}{2\pi} \cdot \left[\arg \left(\sum_{n=1}^{N} A_n e^{i\phi_n} \right) \mod 2\pi \right] \tag{3.13}$$

Where A_n is the weight of every individual beam, meaning it should also be possible to control the intensity for each beam. This ability could be particularly useful for trapping multiple particles or for dumping intensity.

3.2 STED set-up

If we wish to reliably characterize STED doughnuts generated by a SLM, it is important to study them under relevant experimental conditions. For example, we have already discussed that theory predicts the Numerical Aperture has a great effect on the doughnut shape in case of linearly polarized light. Therefore, we have used an actual scanning microscopy set-up with the goal to image fluorescent samples with a doughnut shaped focus, generated by the SLM. For convenience, we will dub this set-up as 'STED set-up' to distinguish it from the previously discussed SLM setup. The STED set-up was an adaptation of a pre-existing set-up where we have made some modifications. From the imaged convolution of the doughnuts with the beads, we should be able to determine if we can predict the doughnut shape. Figure 3.8 shows the STED set-up, which is necessarily more complex than the one used to simply image the focus directly. The
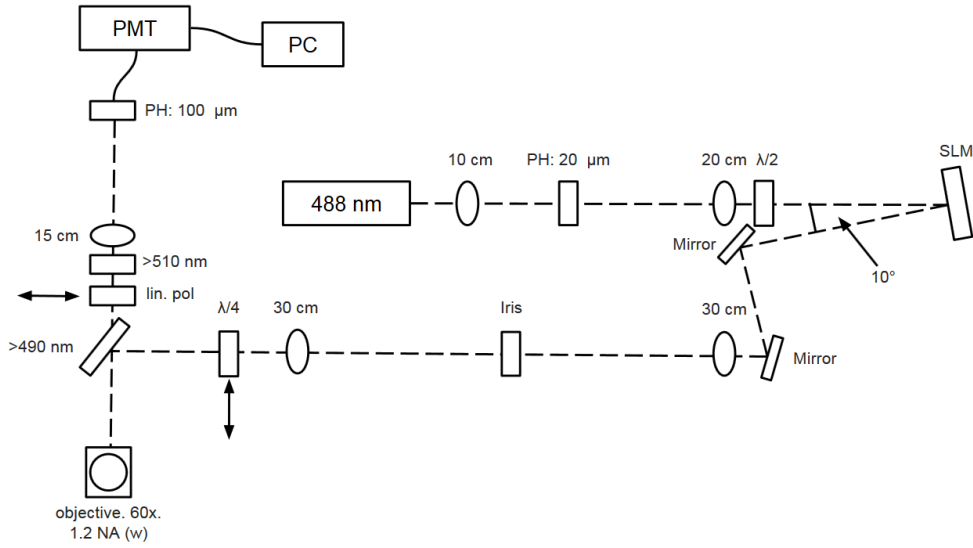
Figure 3.8: Schematic illustration of the set-up. The light emitted by the laser (488 nm) is again expanded. Afterwards, a $\lambda/2$ wave-plate was used to rotate the polarization 90° such that the it would match with the SLM LCD orientation. After modulation, the light is passed through a 4f correlator which an iris in its focus to block the zero-th order. Then, the light would pass through a $\lambda/4$ wave-plate if we wished to generate circularly polarized light. Subsequently, a dichroic mirror would reflect the light towards the Nikon 60x, NA 1.2 water objective where the light was focused on a sample placed on a computer controlled scanning stage. The signal from the sample would be collected by the objective and travel through the dichroic, an optinal linear polarizer and the long pass filter to be focused on a fiber which was connected to a Photo Multiplier Tube, converting the light signal to an electrical signal. Eventually, this electric signal was collected by a computer.

laser used was again an Omicron LuxX®, be it with a lower wavelength of 488 nm. To obtain a larger beam the light emitted from the laser was passed through a beam expander with a pinhole in the focus. Afterwards, the light would pass through a $\lambda/2$ wave-plate in order to rotate the

polarization 90°. This way we obtained horizontally polarized light, such that it matched with the SLM, a different Hamamatsu LCOS-SLM (400-700 nm) which was rotated 90° as well. This was done as it was found that the earlier orientation did not preserve the polarization of the beam, as we will show later. Here, it must be noted that for geometrical reasons, we have used the SLM at an tilt (10°) larger than advised in the manual, which prescribed a maximum tilt of 5°. Fortunately, we initially did not observe any effects resulting from this tilt. As mentioned before, the SLM has a limited efficiency resulting in the zero-th order beam. Hence, On the SLM display, a tilt kinoform was used to separate the reflected and modulated beams. Then, both beams pass through a 4f correlator which was aligned for the first order. Because an iris was placed in the focus, the zero-th order is blocked. Afterwards, the remaining first order could be made circularly polarized by a $\lambda/4$ wave-plate if desired. Regardless of the polarization, the light would enter the objective after being reflected by a dichroic mirror. The objective used was a Nikon 60x, 1.2 NA water immersion objective [25] with a back aperture of 1.0 cm. This objective would focus the light on a fluorescent sample, placed on a stage which could perform a XY scan, controlled by a computer. The objective would also collect the signal emitted by the sample. The emission would subsequently pass through the diochroic and the long pass filter, placed to block the fraction of the excitation light that was reflected from the sample. If desired, a linear polarizer could be placed in front of the long pass filter. Then, the light was focused on a pinhole mend to block environmental light and then coupled onto a fiber which transmitted the signal to the Photo Multiplier Tube (PMT) which converted the signal to an electric signal. Afterwards, this electric signal was amplified and sent to the computer where the images were formed.

Finally, after the set-up was built, it was made operational which meant firstly that we confirmed that the stage was correctly controlled by the computer, as to make sure the XY scan is performed properly. Secondly, the PMT was tested to see whether it converted the signal correctly and that it was properly amplified. Here, it is crucial that the PMT is grounded as it was found that this could generate very strong noise. Thirdly, the set-up had to be very precisely aligned as the doughnuts were observed to be very prone to distortion.

3.2.1 SLM orientation

As we mentioned, we had rotated the SLM 90° for the STED setup, to prevent the SLM from affecting the polarization of the light beam: according to the manual, a tilted SLM should be used in combination with horizontally polarized light such that the polarization direction is parallel to the plane of the tilt of the SLM. If this were not the case, it was observed that the polarization of the light was effected. The polarization of the beam was determined by placing a rotatable linear polarizer in the beam path while measuring the transmittance. In the case of perfectly linear polarized light, we expect the linear polarizer to block all the light if its orientation is at a 90° angle with the polarization of the beam. Figure 3.9 shows the scaled fits of the measured intensities where the black line shows the measured intensity in front of the SLM while the dashed line shows the measured intensity after the SLM. we indeed see the linear polarizer initially blocks
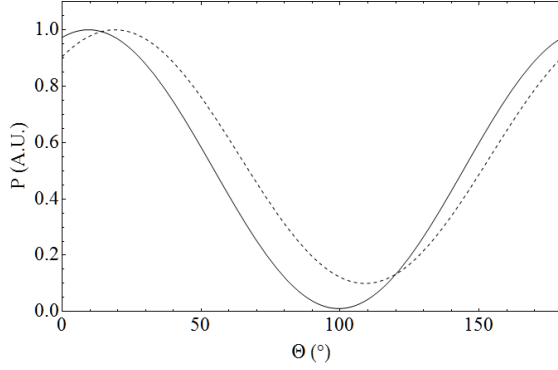
Figure 3.9: Fits of the transmittance of light as a function of the orientation of the linear polarizer. The black line shows the fit from the measurements before the SLM, while the dashed line shows the data from after the SLM. Clearly, after the SLM the light is elliptically polarized and its direction was slightly changed (the position of the maximum and minimum is found at a different angle).

close to 100% of the light, confirming the light was linearly polarized. However, after the light had passed through the SLM, the linear polarizer did no longer block all the light, indicating the light was now elliptically polarized. Additionally, the angle at which maximum transmittance is measured also changed, which means the polarization direction is influenced as well. If the SLM is orientated as advised however, these effects were not observed and the polarizer was able to block practically all the light (98.5% before vs. 98.3% after the SLM).

3.2.2 Sample

The sample that was used in the STED set-up consisted of Fluoresbite® Yellow Green Carboxylate Microspheres with a diameter of 0.2 μm, manufactured by Polysciences [26]. The excitation spectrum of these beads do not reach maximum excitation efficiency at the wavelength of 488 nm that we used, nor could we collect the signal where the emission has its maximum (484 nm) since this is a lower wavelength than the excitation beam. However, we have used this sample anyway because this was the type of microspheres that was available to us at the time the experiment was performed. Moreover, the spectrum shows high emission from 484 nm to approximately 530 nm, meaning we will still collect enough signal even after the long-pass filter at 510 nm. The size of the beads is in the order of magnitude of the expected microscope resolution such that we expect to view the convolution of these beads with the focus.

3.2.3 Experimental details

In the experiment, we wished to image a number of beads using foci with both types of polarization. The images where made by scanning the sample through the focus with a pixel dwell time of 1 ms and a pixel lag of 3.55 ms. Additionally, the highest available resolution of the images was 400x400 pixels. To improve the execution speed of the experiment, we wished to image multiple beads at a time. Unfortunately, this led to a problem because we observed this required scanning regions of $\sim$ 15x15 μm, leading to a maximum pixel pitch of $\sim$ 40 nm. However, we estimated that this would not be a high enough sample rate to accurately measure the small doughnuts. Consequently, we decided to lower the beam diameter to 0.44 cm to reduce the effective NA, which increases the focus size according to eq. 2.6. Moreover, an increased focus size reduces the the effects of the convolution with the beads. Still, this will

also reduce the effects of polarization as these are most prominent for high NA. To illustrate this, if we assume that the effective NA scales linearly with the beam radius, we will obtain an effective NA $0.44 \cdot 1.2 = 0.52$ leaving us at a $\mathrm{NA} = \sin\theta$ of 0.44 in figure 2.12 where the $|E_z|^2/|E_x|^2$ ratio is only ~ 0.1. This means we would also predict an increase of the ratio of the peak to the center of ~ 0.1. Still, we were confident that this difference would be measurable.

The measurements were performed as follows, we would first image a number of beads with both the focus spot as well as the doughnut, using circularly polarized light with the linear polarizer not present. Afterwards, we would continue imaging with a linear polarizer placed in front of the long pass filter as seen in figure 3.8. This way, by measuring in two perpendicular directions, we could determine the polarization of the signal. After these images were made, we would remove the quarter wave plate and repeat these steps with the linearly polarized light. This way, we should be able to determine how the vortex phase influences the shape of the focus, how polarization affects the focus shape and how polarization effects the polarization of the signal. Note that this requires a large number of measurements per beads, and we noticed significant bleaching during the measurements. Fortunately, even with the loss of signal we were still able to perform all the measurement, but this does mean that we cannot properly compare the intensities between the different measurements.

3.2.4 Doughnut model

To compare the shapes of the imaged beads to the theory and determine the quality of the doughnuts, we also simulated the imaging of the beads with the focus. To accomplish this, we first needed a model of the beam shape at the back aperture of the objective such that we can calculate the spot shape using the diffraction integral. To estimate the beam shape, we need to determine the intensity distribution of the beam at the back aperture. To achieve this, we recall that after a pinhole, a beam of light forms a Airy Pattern. Consequently, after the first pinhole shown in figure 3.8, the size of this pattern in front the 20 cm lens is predicted to be:

$$r_{\mathrm{Airy}} = 1.22 \frac{f\lambda}{D} \tag{3.14}$$

where f is in this case the focal length of the lens and D is pinhole diameter. Filling in $f = 20$ cm and $D = 20$ μm, gives a radius of the Airy Disc of 0.6 cm. Next, as we have mentioned we used an iris to reduce the beam diameter to 0.44 cm, such that only the center part of this beam was used. Conclusively, we estimated the beam to be a cutt-off Airy Disc with a radius of 0.44 cm. When we calculated the estimated beam shape, we found that the predicted doughnut size will be slightly larger than it would have been in the case of an uniform bundle, as can be seen in figure 3.10. In contrast, the height of the minimum does not differ significantly. After calculating the focus size, we simulated how the beads are convolved using this focus. For this, we simulated a convolution of the focus with the bead where we have used two models for the bead: a box model and a spherical model. Firstly, for the box model we assumed that the signal as a result of excitation, is the same everywhere on the bead. This is what we expect if the fluorescent molecules are only present on the bead's surface. In contrast, for the second model,

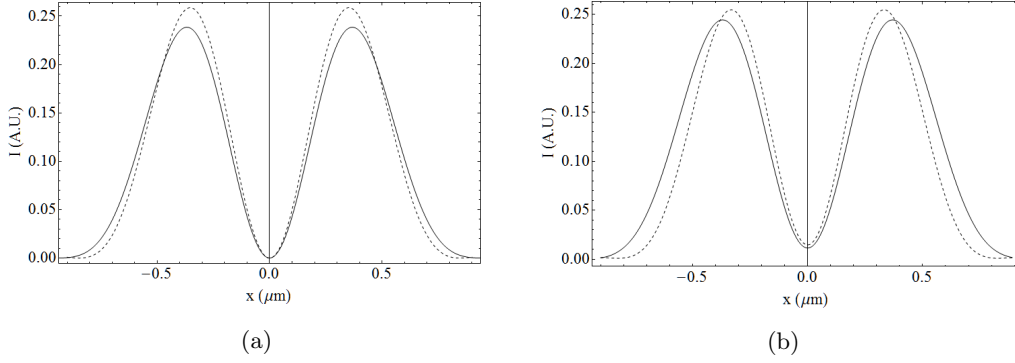(a)   (b)

Figure 3.10:   Diagrams of the predicted donut profiles in case of an uniform (dashed) and Gaussian (solid) bundle. Figure a shows the expected focus profile while the graph in figure b shows the convolution with a 200 nm bead, where the spherical model of the bead was used.
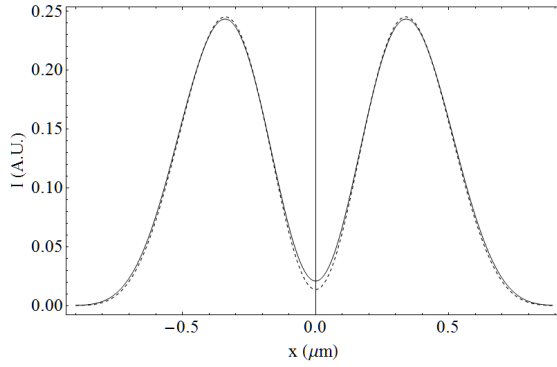
Figure 3.11: Diagram of the predicted convolution profiles in case of a spherical- (dashed) and the box bead model (solid). The two profiles only differ significantly in the center of the doughnut.

we assumed that the signal increases gradually (as a sphere) when approaching the center of the bead meaning that here, we simulate the molecules being present in the entire body of the bead. Figure 3.11 shows the results of the convolution for both models with the previously discussed expected doughnut profile. Here, we see that the shape of both convolutions are mostly very similar but that the height of the expected minima depend greatly on the chosen model. For the sample we have used, we expect the box model to be more closely resembling the beads. These simulations we will use to characterize the measurements where we will specifically look at: the predicted doughnut size and shape compared to the spot size and the intensity in the minimum. Additionally, we will determine and how these criteria are affected by the polarization of the beam.

Chapter 4

Results

We have split the results in two parts: first, we show the results of beam modulation by the SLM, indicating what is possible in terms of beam shaping and giving a starting point for more complex modulation. Second, we show the results obtained from the STED set-up where we have imaged the 0.2 μm beads.

4.1   Beam modulation

We start by showing the images obtained from the camera when a vortex phase kinoform was applied on the SLM. These results will be presented mostly qualitatively because they primarily serve to demonstrate control over the SLM. First, figure 4.1 shows both the reflected- and modulated beam where we have separated the two beams by also displaying a tilt kinoform on the SLM window. From the image, we derived a modulation efficiency of 88% which is very good
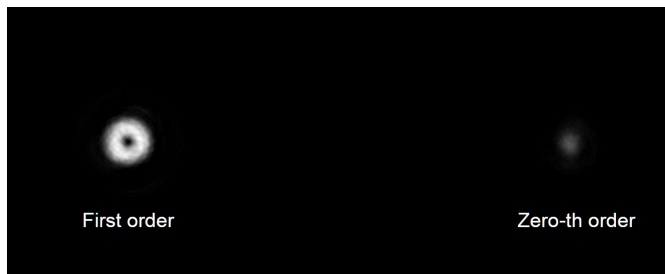
Figure 4.1: Image of the zero-th and first order beams, captured by the camera. The modulation efficiency was determined to be 88%.

given the estimate of the manufacturer of an average efficiency of 82%, indicating that the SLM is a little more efficient at the used wavelength. From the image, the modulated beam seems to have a nice shape comparable to figure 2.11. Additionally, figure 4.2 shows a linear profile of the doughnut of figure 4.1. The profile comfirms that this a very symmetric doughnut with a nice minimum. However, the minimum is not precisely zero, as there was a residual intensity present of 6% of the peak intensity. This is most likely caused by the fact that the measured signal at each pixel originates from the entire area of this pixel, increasing the minimum. Still, it must be confirmed for the final experiments that the minimum is indeed very close to zero as it will obviously

Figure 4.2: Image of the linear profile of the first order, captured by the camera. The center still has an intensity of 6% of the peak intensity.

have an influence on the measurements and our model assumes no residual intensity in the center.

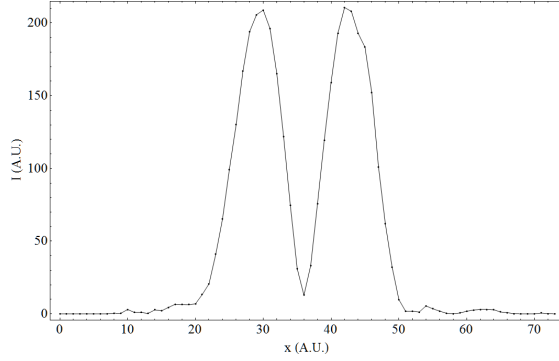Next, we wished to comfirm eq. 3.13 and generate multiple foci on the SLM. Figure 4.3a indeed shows two doughnuts which were created using this method. Both doughnuts were observed to be similar regarding size and shape. Moreover, it is possible to vary A_n between foci as can be seen in figure 4.3b where the lower doughnut contains four times the power of the upper one (we have enhanced the brightness to increase the visibility the upper doughnut). Unfortunately, the creation of multiple foci also increases the presence of the so-called ghost spots, one of which can be seen in the top of figure 4.3a where we note that we have increased the brightness of the ghost spots to improve their visibility. These spots arise because the SLM can only modulate phase and

(a)   (b)
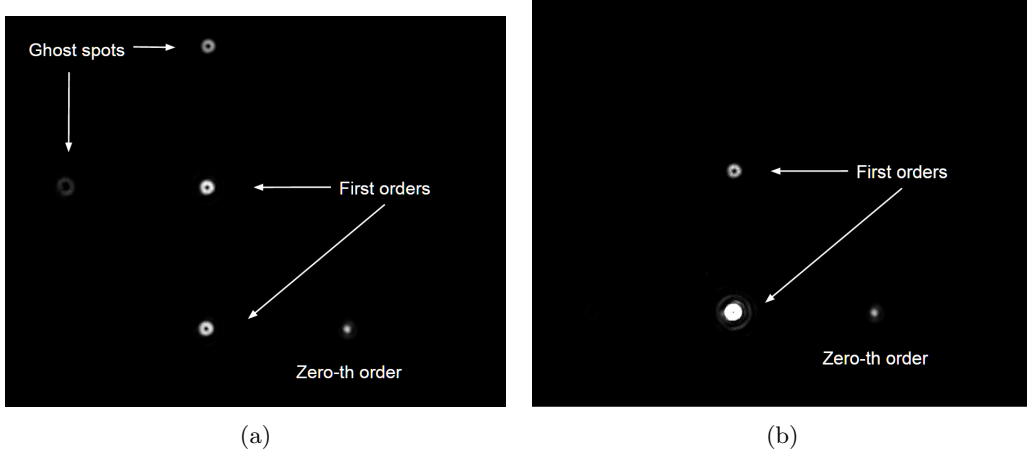
Figure 4.3: Two images showing that the SLM is able to generate multiple foci as well as control their relative intensity. Fig. a shows that the slm can generate multiple foci. Fig. b shows that it is possible to control the relative intensity of these foci, with the lower focus containing 4 times the power of the upper focus. In fig. a, the existence of ghost spots is also apparent.

not intensity such that it is not always able to completely generate the desired intensity distribution in the focus. Not surprisingly, these ghost spots can cause problems if they, for example, unintentionally trap particles during an experiment. Figure 4.4a shows an even better example

with three doughnuts, where the ghost spots actually overlap with the modulated beams, which would be a big issue(See figure 4.4b for the same image with enhanced contrast). Fortunately, a workable solution was found by correction the kinoform $K(\xi, \eta)$, obtaining $K_{corr}(\xi, \eta)$ [24] [27]:

$$K_{corr}(\xi, \eta) = \frac{n_{max}}{2\pi} \cdot [\left| \sum_{n=1}^{N} A_n e^{i\phi_n(\xi,\eta)} \right|^2 \left(\sum_{n=1}^{N} A_n e^{i\phi_n(\xi,\eta)} \right) \mod 2\pi] \tag{4.1}$$

This way, evey component of the combined phase mask is first multiplied by the absolute value of the complex addition of the individual phase masks. The result of this modification can be found in figure 4.4c: the new kinoform has reduced the modulation of the ghost spots, putting them towards the first order and removing their doughnut shape. Moreover, while the modulation efficiency was observed to be lower, the shape of the three doughnuts has remained intact.

(a)

(b)

(c)
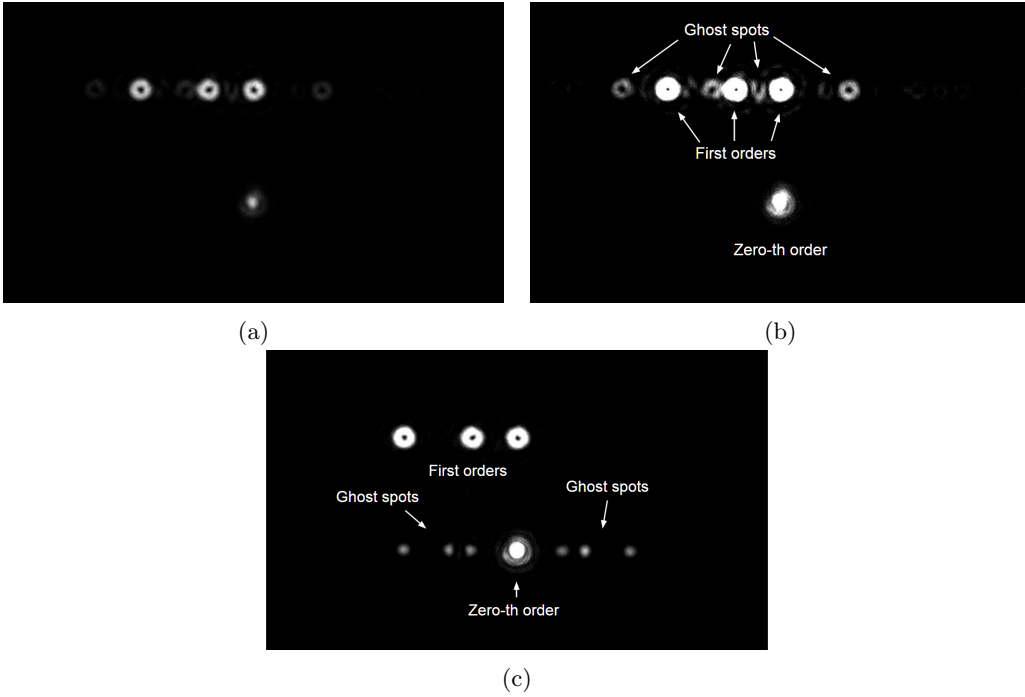
Figure 4.4: Images illustrating the effect of the ghost spot suppression from equation 4.1. Fig. a and b show the initial three modulated doughnut spots with the ghost spots existing partially in between these beams, disrupting the quality (fig. b is the same image with enhanced contrast). Next, fig. 4.4c shows the same modulation with the suppression of the ghosts spots, placing them towards the zero-th order and reducing their intensity.

4.1.1 Gerchberg-Saxton Algorithm

To further test the capabilities of the SLM, we have implemented the Gerchberg-Saxton algorithm to generate a very unusual intensity distribution in the focus; a house including a window and a door, all desired to have the same intensity. As source intensity, we approximated the beam profile as a Gaussian and we used a random initial phase ϕ_o. In this experiment, we have not used a threshold δ, since we found that the algorithm did not improve the focus quality after 30 iterations. To illustrate this, figure 4.5a shows the result from 30 iterations while figure b has had 60. Apparently, these extra 30 iterations do not seem to have brought any noteworthy improvements. To confirm this, an attempt was made to quantify the quality of the patterns. This was done by measuring the variance of the intensity in an area of the image. By dividing the variance by the mean intensity of the area, we could say something about the quality of the focus as we desired an uniform intensity. This method is by no means perfect, but at least gives us a quantitative result. For 30 iterations, this ratio was found to be 0.55 while 60 iterations gave a ratio of 0.59. In both cases, this indicates that the profile fluctuates rather significantly but that after 30 iterations no further improvement comes from the extra iterations. In this case, the quality was actually worse. From the images, these fluctuations are visible as distortions and

| (a) | (b) |
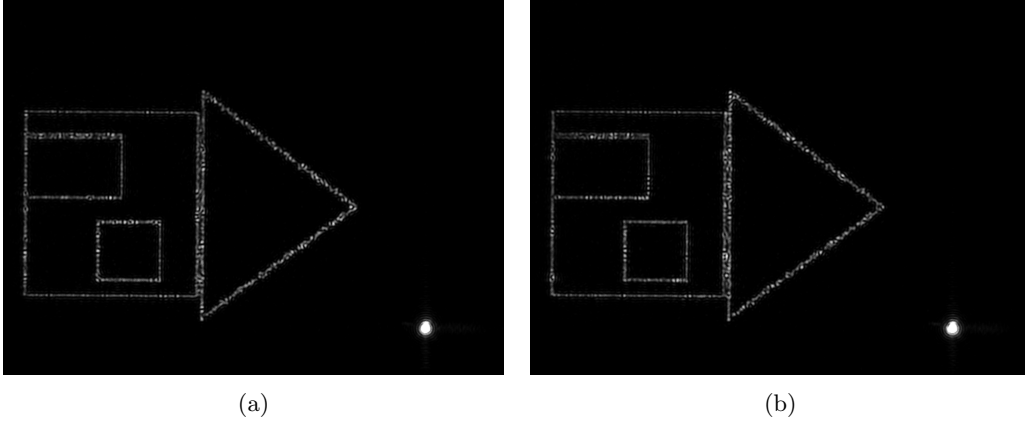
Figure 4.5: Two images showing the results of Gerchberg Saxton algorithm. Fig. 4.5a has had the algorithm do 30 iterations, while fig. 4.5b has had 60. Image size is 7.18x5.32 mm (the size of the camera sensor).

speckles with 100% contrast. In the future, if we wish to create distributions where the quality is very important (arrays of STED doughnuts, for example), these speckles are a major concern. Additionally, these speckles were seen regardless which shape we tried to generate. Since this is not the primarily subject of this thesis, we will only discuss the possible sources of these speckles (and their possible solutions) shortly. To start, one aspect we noticed was the large effect of the approximation of the source intensity, as can be seen in figure 4.6. Here, from figure 4.6a to figure 4.6d gradually increased the radius of the estimated source intensity from 0.5x, 0.75x, 1.0x the standard deviation of the actual Gaussian profile to a perfectly uniform bundle (the actual source intensity remained constant). From these images, the results are observed to improve

when the estimated source intensity is closer to the actual value while the result generated with the completely uniform bundle shows again more distortion. On the other hand, the result from figure 4.6a seems to posses some nice profiles at certain points, but appears blurred and incomplete on others. These findings are confirmed by the measured ratio of the variance of the intensity divided by its mean, visible in table 4.1. Interestingly, when the calculated phase masks

	Ratio intensity variance/mean
0.5 SD	0.88
0.75 SD	0.55
1.0 SD	0.47
uniform	0.68

Table 4.1: Table indication the fluctuations in the pattern depending on the estimated initial intensity distribution. Lower values mean less flunctuations.

were Fourier transformed, it was found that the best results are obtained if the phase mask is combined with an uniform bundle, even if the algorithm had assumed a non-uniform bundle. we might explain this by understanding that no matter what the algorithm does, an uniform bundle fully utilizes the SLM display such that every component the kinoform is equally represented. However, in the case of a Gaussian bundle, the kinoform components on the outer part of the SLM window are not fully present in the focus. Therefore, we suggest to use a large top-hat beam to improve the modulation of the light. Moreover we must realize that the displayed kinoforms are discrete and necessarily do not contain the all information. Unfortunately, we do not expect these observations to fully solve the speckle problem: the source of these speckles most likely lies in the fact that we can only control the phase of the light and not the intensity. As a result, the phase distribution causes interference resulting in dark speckles similar to the manner we create the minimum for the doughnuts. These complex distribution can only be accurately obtained if both phase and amplitude are controlled, such that we have approximately an uniform phase in the focus. Currently, multiple methods have already been proposed to achieve this, either by using one or two SLM's to control the phase in both planes, using superpixels [28], smoothing constraints [29],or by spatially averaging multiple kinoforms [30]. However, these methods are quite complex and beyond the scope of this research. Here, our goal was to achieve good control over the SLM and understand how it modulates light. Now that we have established this, we will continue to the results of the doughnut analysis.

<div align="center">(a)</div>   <div align="center">(b)</div>

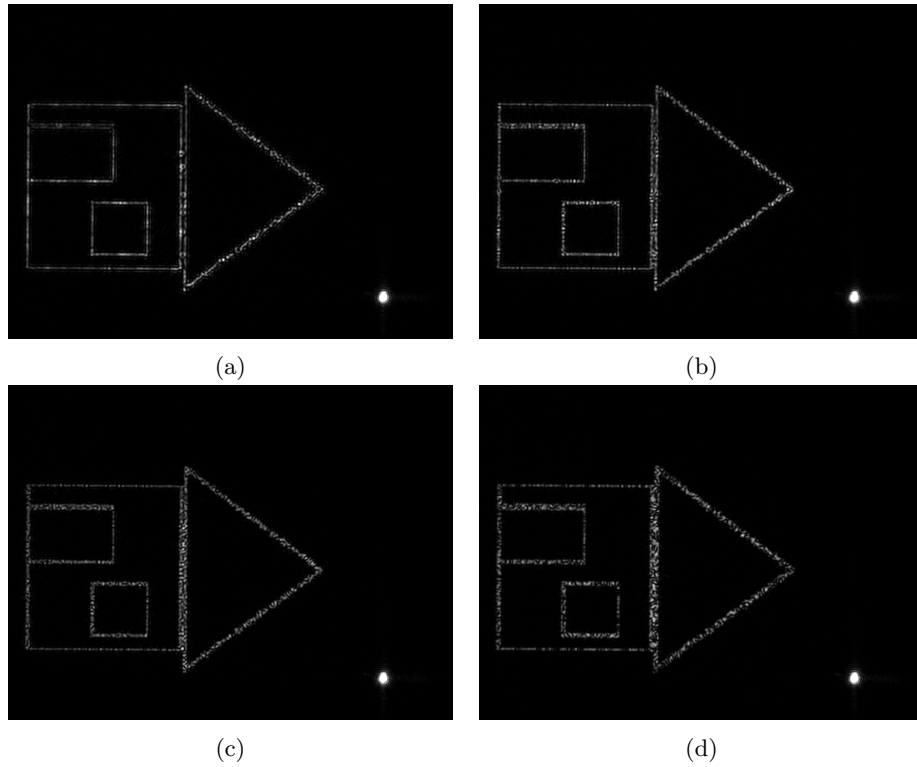<div align="center">(c)</div>   <div align="center">(d)</div>

Figure 4.6: Results from the Gerchberg-Saxton algorithm where the initial intensity was estimated to be a Gaussian with: $0.5SD$ (a), $0.75SD$ (b) and $1.0SD$ (c) where SD is the actual measured standard deviation of the beam. Figure 4.6d is the result where an uniform intensity was estimated. Image size is 7.18x5.32 mm.

4.2 Doughnut Analysis

Before we imaged the beads with the STED set-up, we had imaged the reflection of the doughnut by temporarily removing the fiber (coupler) and placing a camera in the focus of the 15 cm lens (see figure 3.8). A result can be seen in figure 4.7. From this, we established that the center of the doughnut had a nice zero and possessed good symmetry. Next, the results from the STED
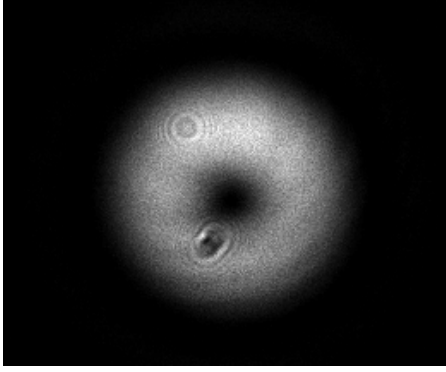

Figure 4.7: Image of the doughnut on the camera placed in the focus of the 15 cm lens seen in figure 3.8, after it has passed through the objective where it was reflected. The measured intensity in the center is zero. The distortions seen on the image originates from dust on the camera sensor.

set-up were obtained from the sample in three scanning sessions where a total 13 beads were imaged thoroughly (4, 6 and 3 beads for each session respectively). The beads were imaged with a sample rate of one pixel every 50 nm for the first and the third sessions while a rate of one pixel every 75 nm was used for the second session. This was the case, because we imaged a larger area where this was the maximum obtainable pixel pitch (see the front of the thesis for an image of the second session). Firstly, figure 4.8 shows both 'wide-field'- and closeup images of the four beads from the first session. Here, sub-figures 4.8a and 4.8c were created with an uniform phase, showing regular convolution spots. In contrast, figures 4.8c and 4.8d show the same beads now imaged with the vortex phase kinoform displayed on the SLM window. In both cases, the light was circularly polarized, which predicted the best doughnut shapes.

4.2.1 Doughnut size

For the quantitative analysis, we first determined the size of the beads in the images. This way, we can verify that these beads were imaged in focus and confirm whether our theoretical predictions of the bead size is correct. In order to determine the size of the beads, radial profile plots of the beads were made in ImageJ [31], using a custom plugin called 'Radial Profile Plot' [32]. These profiles were obtained by averaging the measured intensity at increasing radii from the center of the bead:

$$I_{avg}(r) = \frac{1}{2\pi r} \sum_{\theta=0}^{2\pi} I(\theta, r) \tag{4.2}$$

This way, angular asymmetries were averaged out leaving better profiles. However, the averaging over discrete pixels and possible mistakes in pinpointing the center of the bead can result in errors in the profiles. Still, this method was found to be more reliable than traditional cross section
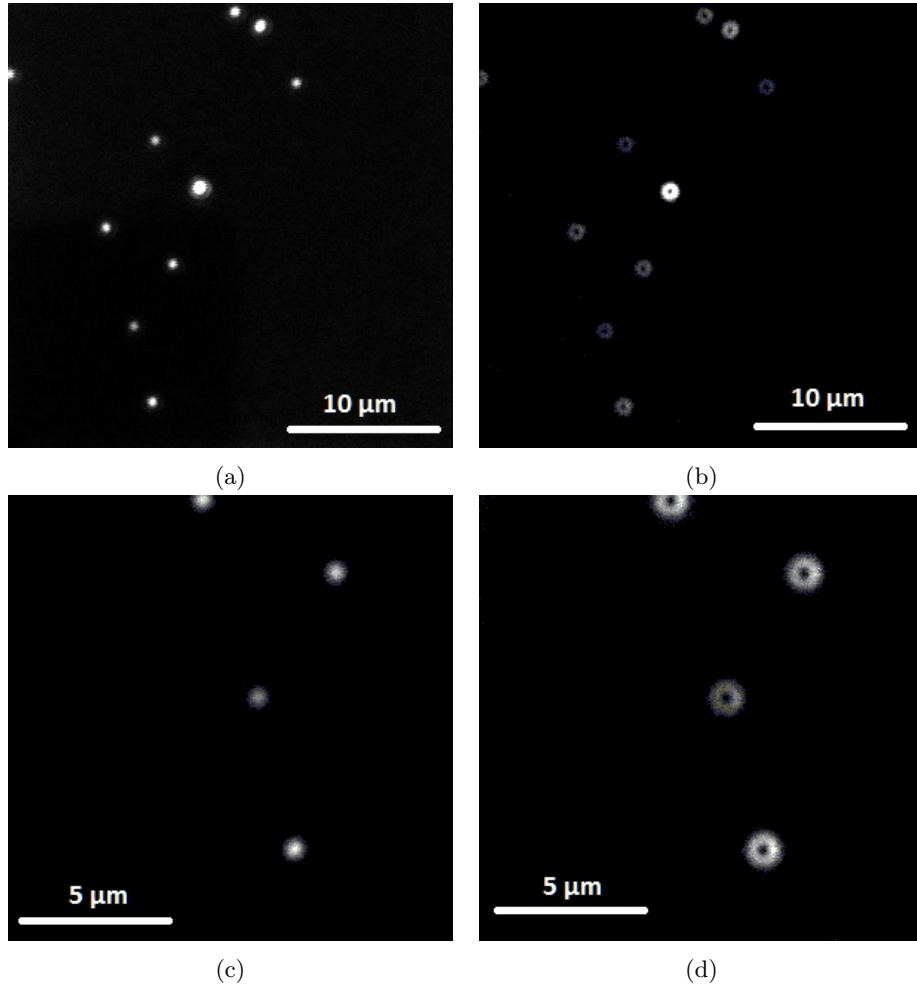
Figure 4.8: Images of the 200 nm fluorescent beads with, made with both an Airy Disc (a & c) and a doughnut shaped focus (b & d). b & d are closeups of the lower left corners of image a & c. In all cases, the focused light was circularly polarized.

line profiles as the radial profiles provided very similar profiles for all the beads. Initially, when the obtained profiles were compared to the theoretical predictions, it was observed that all the measured spots were approximately 11% smaller than the predicted radius. To explain this, we need to take several things into account.

- The discrepancy cannot be explained by suggesting the images were taken out of focus, since this would have increased the measured radius.

- Possible mistakes in the estimated beam shape (Gaussian vs. Uniform) in the back aperture cannot explain an error of this magnitude, as can be seen in figure 3.10 where the peak to peak distances differ only 3%.

- The discrepancy was present in the line profiles as well, which means that it can not have been an error in the radial profiles it.

Consequently, we suspect that the calculation of the effective NA is not valid, which may be because the approximation of eq. 2.5 does not hold in this case, which is sometimes suggested in literature [33] but also rejected [14]. Therefore, future research will be required to establish the true relation between NA and beam radius. Fortunately, in this experiment, we were mostly interested the effect of the vortex phase mask on the beam, meaning we only wish to know how the beam profile is changed compared to the initial focus spot. Therefore, we decided that it is reasonable to correct the theoretical prediction of the spot size to fit experiment, which resulted in the figure 4.9. we did this by increasing the effective Numerical Aperture with 11%. Here, the black line shows the corrected model while the coloured lines shows cross sections of the spots seen in figure 4.8c. With the corrected model established, figure 4.10a again shows in black the
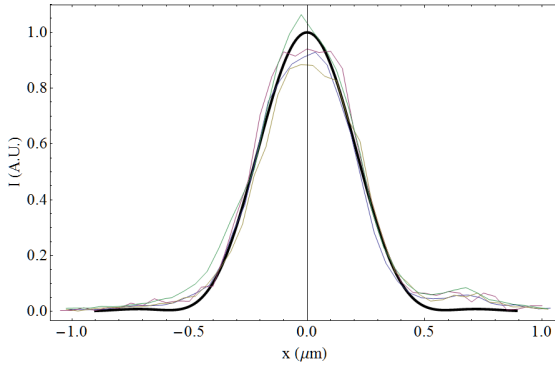
Figure 4.9: Figure showing the cross sections of the spots shown in figure 4.8c and the corrected fit which predicts the shape. The line profile is shown, rather than the radial profile because the line profile has a better defined x−axis.

(corrected) theoretical model compared to the measured radial profiles of the four beads seen in figure 4.8c where the intensity is scaled to 1.0 for $r = 0$. Clearly, with the correction there is an acceptable agreement between data and theory. More importantly, figure 4.10b shows the radial profile plots of the doughnuts where the intensities are scaled by measured intensities of the spots. Here, the same correction was used as for the spots. From this image, again it can be observed that the theoretical model agrees quite well with the measured size of the doughnut. Note, that in figure 4.10b the height of the model was fitted to the data as bleaching has reduced

<center>(a)</center>

<center>(b)</center>

Figure 4.10: Figures showing the radial profiles (coloured) of both the spots (fig. 4.8c and the doughnuts (fig. 4.8d) compared to the model laid out in this thesis (black). Note that the intensity of model is fitted to the measured profiles to counter the effects of bleaching. Also, the green profile represent is the upper bead which was only partly imaged, which might explain why a deviation from the norm.

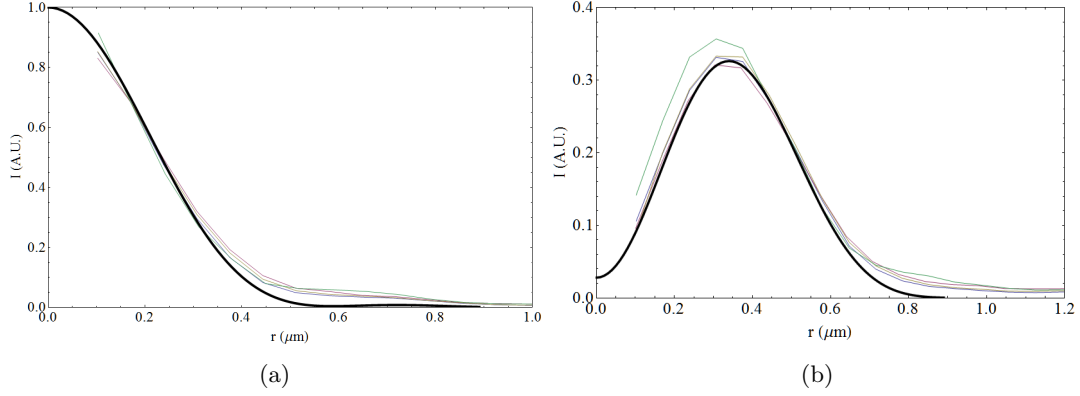the intensity measured. At first sight, it seems that if the spot size is known, our current model can quite accurately predict the shape of the doughnut. Still, the measured profiles seem to deviate slightly near the edges of the foci. This phenomenon we cannot explain, but as we will see they are, to a lesser extent, also present in the linear profiles as well (for example the blue profile in figure 4.13a). To get better insight in the size of the beads compared to the model, the peak of the radial profiles were fitted with a parabola and the position of the maximum was determined. Then, these results were used to get an approximation of the Peak-Peak distance of every doughnut. The results can be seen in table 4.2 for beads imaged with both circularly- and linearly polarized light. From the new model, the predicted Peak-Peak distance is 0.68 μm, which is in good agreement with the measured P-P distances for the circularly polarized foci. Interestingly, the fits of the beads illuminated with linear polarized show slightly but significantly smaller P-P distances. A possible explanation for this will follow later.

4.2.2 Center minimum

Next, we wish to verify the predicted effects of polarization on the shape of the doughnut. First, figure 4.11 shows three beads (11, 12 & 13) imaged both with linearly and circularly polarized light. From these images, it is already clear that the intensity in the center is much less in the case of circularly polarized light. This is even more clear from figure 4.12 which shows the vertical line profiles of both sets of doughnuts. Here, figure 4.12b shows a much worse minimum than figure 4.12a. Again, the black line gives the predicted doughnut shape and size of the corrected model. To quantify these findings, we determined the ratio between the maximum intensity and minimum intensity for every bead imaged both by linearly- and circularly polarized doughnut. The maximum intensity was taken from the radial profiles, such that it the maximum was an average over all angles. Subsequently, the minimum was found by averaging the found minima

	P-P circular (μm)	P-P linear (μm)
Bead 1	0.66	0.65
Bead 2	0.66	0.65
Bead 3	0.67	0.65
Bead 4	0.63	0.65
Bead 5	0.67	0.61
Bead 6	0.68	0.64
Bead 7	0.68	0.62
Bead 8	0.66	0.61
Bead 9	0.67	0.64
Bead 10	0.69	0.62
Bead 11	0.66	0.64
Bead 12	0.68	0.65
Bead 13	0.68	0.64
Average	0.67$\pm$0.01	0.64$\pm$0.02

Table 4.2: The measured P-P distance for every bead measured both with linearly- and circularly polarized light. The errors shown in the average are standard deviations showing the spread of the measured quantity among all the beads.

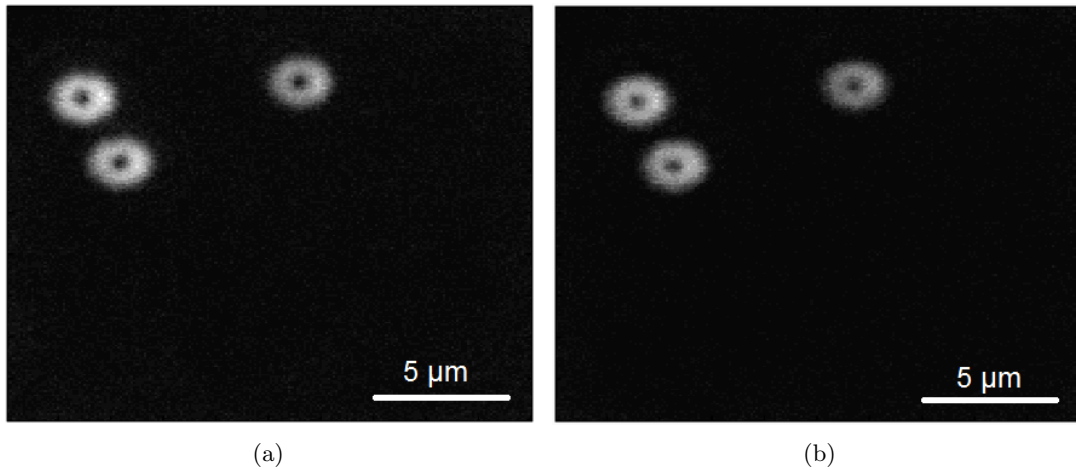(a)   (b)

Figure 4.11: Two images of beads of the third session; fig. 4.11a was imaged with circularly polarized doughnuts, while fig. 4.11b shows the resulting image of linearly polarized light.

of both the vertical and horizontal linear profiles of each bead. The results are found in table 4.3. Now, the predicted min/max ratio for the corrected model was found to be 0.085. If the measured ratio is compared to the predicted ratio, we see that overall, the measured ratio is significantly higher than predicted. However, this is to be expected since the measured minima are actually summed intensity originating from at least 50x50 nm area (one pixel). Furthermore, since the scanning is done in discrete steps of at least 50 nm it is very likely that during a scan,

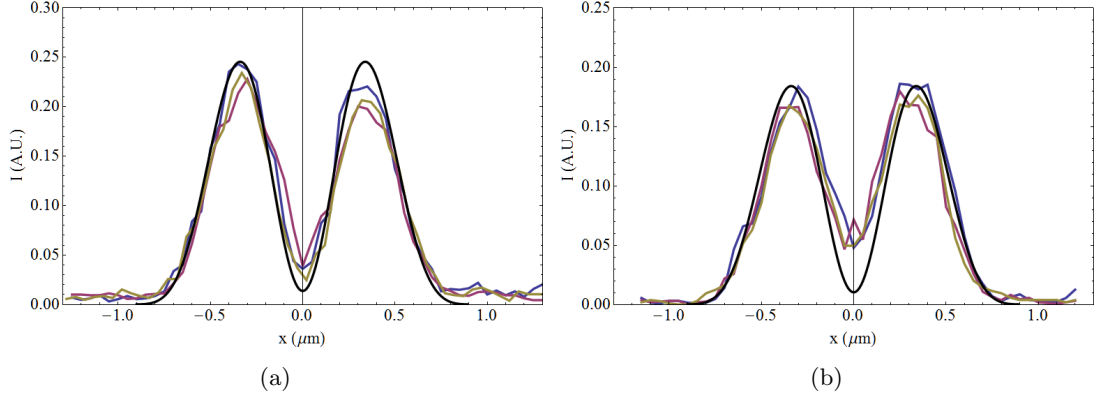(a)   (b)

Figure 4.12: Figures showing the linear profiles (coloured) of both the circularly (fig. 4.11a) and horizontally (fig. 4.11b) polarized light compared to the model laid out in this thesis (black).

the minimum of the focus never falls exactly on the center of a bead. As a result, the average will always lie slightly higher than the predicted minimum. In contrast, with these things in mind, all the beads do posses very similar ratio's, increasing our confidence in the measurements (note that the pixel size of beads 5-10 was different). Additionally, despite the resolution limits it can be clearly determined that ratio of the minima and maxima was consistently worse in the case of linearly polarized light, as theoretically predicted. To recall, in the case of linearly polarized light, we expected the intensity in the minimum to increase approximately by 0.1 the peak intensity which, compared to the measured averaged increase of 0.12, suggests that even the amount of increase agrees quite well with theoretical predictions. In fact, we probably had a higher effective NA due to the earlier discussed discrepancy in the size of the spots, which would have brought the predicted increase even closer to the measured one. However, it must be noted that the results in table 4.3 seem to suggest that the image resolution has had a large effect on the measurements as beads 5-10 show significantly higher ratio and a higher increase, which means we cannot boldly state to have observed precisely the predicted increase. Still, we can certainly conclude that linear polarized light produces a worse minimum.

4.2.3 Polarization effects on the focus shape

A bigger challenge than the previously discussed would be to see if we can also observe the expected increase in asymmetry in the case of linearly polarized light. As discussed earlier, we expect an increase in the intensity in the direction perpendicular to the polarization direction which in our case, is the direction of $y-$axis. Firstly, we must note that the doughnuts were not totally symmetrical in the case of circularly polarized light, as can be seen from figure 4.13a which shows the average of the horizontal (red) and vertical (blue) line profiles of the beads from figure 4.8. Apparently, the doughnuts possessed a higher average intensity in the horizontal direction as well as an asymmetry. Regardless, we can still determine any possible effects of the polarization by comparing the profiles. Interestingly, the expected increase of the intensity in the vertical direction should in our case, partially cancel the initial aberation leaving a more

	center/peak circular	center/peak linear	Increase (%)
Bead 1	0.15	0.26	72
Bead 2	0.09	0.22	157
Bead 3	0.17	0.24	44
Bead 5*	0.16	0.37	127
Bead 6*	0.17	0.37	115
Bead 7*	0.20	0.43	115
Bead 8*	0.21	0.45	110
Bead 9*	0.20	0.41	111
Bead 10*	0.16	0.35	115
Bead 11	0.14	0.24	64
Bead 12	0.17	0.31	80
Bead 13	0.13	0.30	141
Average	0.14±0.03	0.26±0.03	86±6

Table 4.3: The measured ratio's between the maxima and minima for each bead. The results from beads 5-10 were not used for the average, as the data is apparently influenced by the lower sample rate.
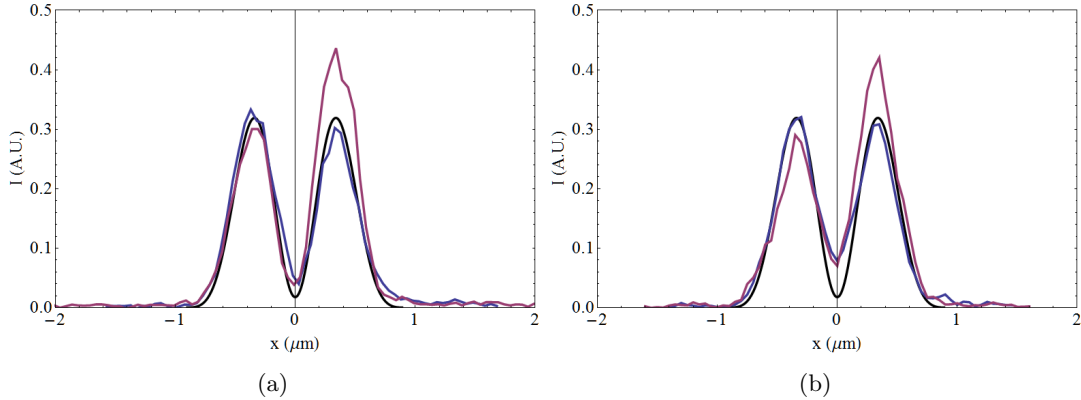

Figure 4.13: Images comparing the averaged vertical and horizontal line profiles for both polarizations for the first scanning session. Fig. a shows the results for the circularly polarization with in red, the horizontal- and in blue the vertical profile. Next, fig. b shows the results from linearly polarized light.

symmetrical doughnut. Indeed, if we look closely at figure 4.13b we see the horizontal profile is reduced compared the vertical profile, albeit slightly. Table 4.4 shows the measured ratio of the horizontal maximum to the vertical profiles, confirming the initial asymmetry as all beads posses higher maxima in the horizontal direction. Indeed, in the case of linear polarized light, we see a reduction of this ratio, implying that the maxima in the direction perpendicular to the polarization direction have indeed increased. Additionally, as we have already observed, we can see in figure 4.13 that the size of the bead is slightly decreased in the case linear polarized

light. More precisely, it seems the radius of the bead in the vertical direction is smaller. If we again look back at figure 2.11, this is indeed what we expect. This might explain why we earlier observed that the radial profiles of in the case the linear polarization were slightly smaller.

Table 4.4: Table showing the ratio of the peak intensities for both types of polarization.

	horizontal/vertical circular	horizontal/vertical linear	linear/circular
Bead 1	1.13	1.06	0.93
Bead 2	1.18	1.07	0.91
Bead 3	1.12	1.04	0.93
Bead 5	1.23	1.07	0.87
Bead 6	1.11	1.01	0.91
Bead 7	1.20	1.11	0.93
Bead 8	1.16	1.04	0.90
Bead 9	1.23	1.12	0.91
Bead 10	1.18	1.10	0.94
Bead 11	1.14	1.04	0.92
Bead 12	1.11	1.06	0.96
Bead 13	1.13	1.05	0.93
Average	1.135±0.023	1.053±0.012	0.93±0.016

4.2.4 Polarization of the emission

Finally, we will discuss the measured polarization of the fluorescent signal. Figure 4.14 shows two of these images where we compare the doughnut shape for both polarization directions. Apparently, both images show some distortion of the doughnut, most likely caused by the addition of the polarizer which must have shifted the beam slightly. Still, the images are very similar indicating that the polarization of the emission is independent of the excitation. Furthermore, rotating the linear polarizer did change the distortion but it did not introduce a noticeable difference between the two polarization directions. Additionally, we also did not observe an intensity dependence on the orientations of the linear polarizer, leading us to suspect that the emission is not polarized, independent of the polarization of the excitation .

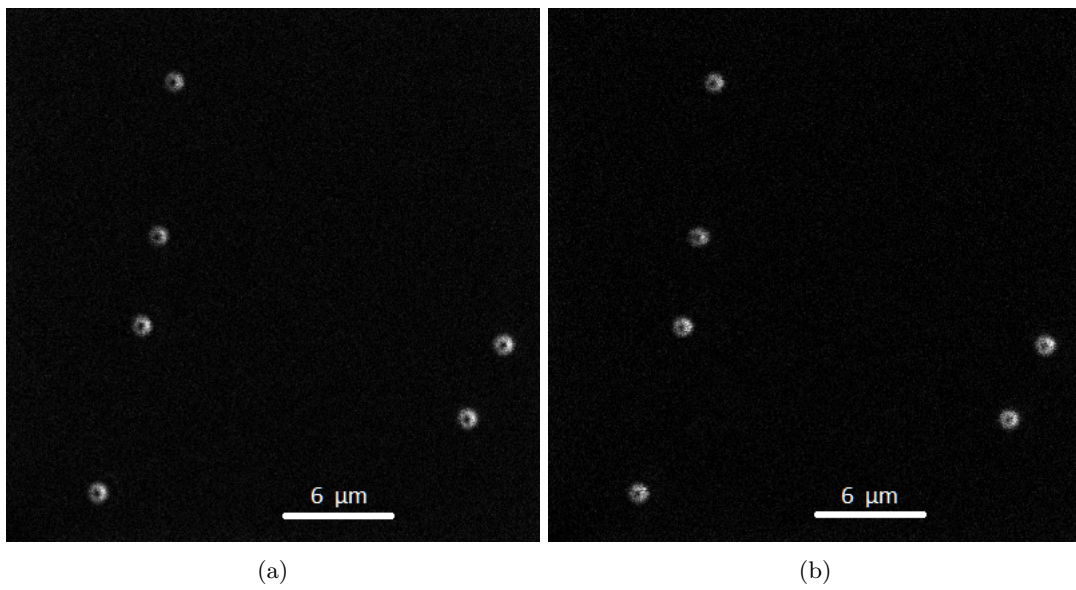(a)   (b)

Figure 4.14: Two images showing the signal retrieved with a linear polarizer placed in the emission path. Fig. a shows the results for circularly polarized light, while fig. b shows the same beads imaged with linearly polarized light.

Chapter 5

Discussion & Outlook

Firstly, we can confirm that phase-only LCOS SLM's are a viable and flexible option for beam modulation and STED doughnut generation as these devices have shown efficient and accurate beam modulation while also being very user-friendly. Besides, the effects of these SLM's in the case of simple kinoforms is predictable, increasing the usability. The biggest problem with these devices have been the reported ghost spots which can, in many situations, be a major problem. However, in the case of microscopy where only a separation from the non-modulated beam is desired these unwanted spots are easily blocked with a mid-focus. Moreover, we have already shown one method that can help reducing the problems caused by the presence of these ghost spots.

If we look at the quality of the doughnut-shape foci in the STED environment, we have seen that the doughnuts posses an acceptable center minimum and posses a nice, symmetrical shape, indicating that the SLM was very capable of generating the doughnuts. Still, one significant aberration was observed in the form of an increased intensity positioned on the ring of the doughnut. We think this aberration might have been caused by the fact that the angle of the SLM was bigger than advised. This may have resulted in the asymmetry in the focus shape. Therefore, we would advice to design a future set-up where the angle of incidence of the light on the SLM display is sufficiently small ($< 5°$). Also, we were unable to obtain fully circularly polarized light with the used $\lambda/4$ wave plate where we could measure a horizontal/vertical polarization ratio of 1.16 where the desired ratio is 1.0. If a better wave plate is used, preferably one manufactured specifically for the used wavelength, more accurate results could be obtained.

In the experiment, we have indeed observed the expected polarization effects both qualitatively and quantitatively. We can conclude that linearly polarized light is not desired for good quality STED, as we have seen that linearly polarized light has an increased center intensity even in the case of a relatively low effective Numerical Aperture. Furthermore, the model used to describe the focus shape showed good agreement with experiment.

Still, we were not able to fully quantify and therefore confirm the exact effects from polarization as the measurements were not precise enough. Therefore, more research will be needed: first, because we have not been able to fully predict the effect of the beam radius on the focus size, we suggest to first device an experiment where this relationship is measured, for one or more objectives. In fact, after this experiment one should be able to quantify the effects of NA on the deformation of the doughnut in the case of linear polarized light and see if this confirms simulations. Furthermore, if the polarization effect are to be made more quantitative, we would advise to use a smaller sample and a higher NA to increase possible polarization effects. However, this will reduce the focus size significantly increasing the difficulty of the experiment. Moreover, this will require a much higher sample rate as well, because this is necessary for a more accurate analysis of the beam shape and the center intensity. To partly counter the need for a higher sample rate, one could use light of a higher wavelength, as this will again increase the focus size. Additionally, the size of the SLM window limits the maximum beam radius one can use unless an extra beam expander is used after the SLM. Finally, it might also be interesting to measure the focus shape with the wrong circular polarization direction to see how this affects the doughnut shape. This is interesting, because others have shown that the current simulations might not give accurate predictions [14].

Hopefully, with the foreknowledge of this thesis and the experimental set-up in place, future experiments can consist of detailed quantitative measurements of the shape of the foci, with the potential of greatly helping future STED experiments.

Chapter 6

Acknowledgements

First, I would like to thank the Molecular Biophysics group for allowing me to use their material, an office and the coffee machine, saving me quite some money. Next, I would like to give my gratitude to Dave van den Heuvel for his help with the various electrical devices when they stopped showing signs of life. Then, I like to thank Peter van der Straten for his willingness to correct this thesis. Also, I must thank Gerhard Blab for being my daily supervisor, speaking to me regularly and helping me out with various problems. Last but not least, I must really thank Imaad Mohammed for helping me on a daily basis with building the set-up and getting it operational: it must have cost him quite some time over the length of the year and I felt that at certain days, his help on my thesis eclipsed his own work. For his constant support I am truly grateful.

Bibliography

[1] Dr. E.D. Pijzel. Antony van leeuwenhoek. *De Gids*, 1875.

[2] Dr. A. van Leeuwenhoek. Letter to H. Oldenburg, 1957.

[3] George Biddell Airy. On the diffraction of an object-glass with circular aperture. *Transactions of the Cambridge Philosophical Society*, 5:283, 1835.

[4] Image taken from `http://coinimaging.com/images/airy-disc.jpg`.

[5] O'Haver. Intro to signal processing - deconvolution. 2007.

[6] Dr. G.A. Blab. Superresolution microscopy, 2014.

[7] Diagram taken from `https://www.lifetechnologies.com/nl/en/home/life-science/protein-biology/protein-biology-learning-center/protein-biology-resource-library/pierce-protein-methods/fluorescent-probes.html`.

[8] Dominik Wildanger, Brian R Patton, Heiko Schill, Luca Marseglia, JP Hadden, Sebastian Knauer, Andreas Schönle, John G Rarity, Jeremy L O'Brien, Stefan W Hell, et al. Solid immersion facilitates fluorescence microscopy with nanometer resolution and sub-ångström emitter localization. *Advanced Materials*, 24(44):OP309–OP313, 2012.

[9] Joseph W Goodman. *Introduction to Fourier optics*. Roberts and Company Publishers, 2005.

[10] Max Born and Emil Wolf. *Principles of optics: electromagnetic theory of propagation, interference and diffraction of light*. Cambridge university press, 1999.

[11] Eugene Hecht. Hecht optics. *Addison Wesley*, 997:213–214, 1998.

[12] George Neville Watson. *A treatise on the theory of Bessel functions*. Cambridge university press, 1995.

[13] Jonathan Leach, Eric Yao, and Miles J Padgett. Observation of the vortex structure of a non-integer vortex beam. *New Journal of Physics*, 6(1):71, 2004.

[14] Bhanu Neupane, Fang Chen, Wei Sun, Daniel T Chiu, and Gufeng Wang. Tuning donut profile for spatial resolution in stimulated emission depletion microscopy. *Review of Scientific Instruments*, 84(4):043701, 2013.

[15] Djenan Ganic, Xiaosong Gan, and Min Gu. Focusing of doughnut laser beams by a high numerical-aperture objective in free space. *Optics express*, 11(21):2747–2752, 2003.

[16] K Bahlmann and SW Hell. Electric field depolarization in high aperture focusing with emphasis on annular apertures. *Journal of microscopy*, 200(1):59–67, 2000.

[17] Xiang Hao, Cuifang Kuang, Tingting Wang, and Xu Liu. Effects of polarization on the de-excitation dark focal spot in sted microscopy. *Journal of Optics*, 12(11):115707, 2010.

[18] Saxton W O Gerchberg R W. A practical algorithm for the determination of phase from image and diffraction plane pictures. *Optik*, 35:237, 1972.

[19] Elroy P. Using the spatial light modulator for adaptive optics in fluorescence microscopy.

[20] Product details can be found at `http://www.hamamatsu.com/jp/en/X10468-07.html`.

[21] Eric R Dufresne, Gabriel C Spalding, Matthew T Dearing, Steven A Sheets, and David G Grier. Computer-generated holographic optical tweezer arrays. *Review of Scientific Instruments*, 72(3):1810–1816, 2001.

[22] Chao Li, Mingliang Xia, Quanqun Mu, Baoguang Jiang, Li Xuan, and Zhaoliang Cao. High-precision open-loop adaptive optics system based on lc-slm. *Optics express*, 17(13):10774–10781, 2009.

[23] Jung-Ping Liu, Wang-Yu Hsieh, Ting-Chung Poon, and Peter Tsang. Complex fresnel hologram display using a single slm. *Applied optics*, 50(34):H128–H135, 2011.

[24] R Bowman, V DAmbrosio, E Rubino, O Jedrkiewicz, P Di Trapani, and MJ Padgett. Optimisation of a low cost slm for diffraction efficiency and ghost order suppression. *The European Physical Journal Special Topics*, 199(1):149–158, 2011.

[25] a Nikon VC 60XWI, product details can be found at `http://www.nikoninstruments.com/en_EU/Product-Selectors/Objective-Comparison/(items)/i94`.

[26] `http://www.polysciences.com/default/fluoresbrite-yg-carboxylate-microspheres-020m`.

[27] Joseph P Kirk and Alan L Jones. Phase-only complex-valued spatial filter. *JOSA*, 61(8):1023–1028, 1971.

[28] EG Van Putten, IM Vellekoop, and AP Mosk. Spatial amplitude and phase modulation using commercial twisted nematic lcds. *Applied optics*, 47(12):2076–2081, 2008.

[29] Frank Wyrowski and Olof Bryngdahl. Iterative fourier-transform algorithm applied to computer holography. *JOSA A*, 5(7):1058–1065, 1988.

[30] Lior Golan and Shy Shoham. Speckle elimination using shift-averaging in high-rate holographic projection. *Optics express*, 17(3):1330–1339, 2009.

[31] Website of Fiji Is Just ImageJ: `http://fiji.sc/Fiji`.

[32] Developed by Paul Baggethun: `http://rsb.info.nih.gov/ij/plugins/radial-profile.html`.

[33] Fritjof Helmchen and Winfried Denk. Deep tissue two-photon microscopy. *Nature methods*, 2(12):932–940, 2005.